



Authigenic berthierine and incipient chloritization in shallowly buried sandstone reservoirs: Key role of the source-to-sink context

Maxime Virolle, Benjamin Brigaud, Daniel Beaufort, Patricia Patrier, Eid Abdelrahman, Hadrien Thomas, Eric Portier, Yann Samson, Raphaël Bourillot, Hugues Féliès

► To cite this version:

Maxime Virolle, Benjamin Brigaud, Daniel Beaufort, Patricia Patrier, Eid Abdelrahman, et al.. Authigenic berthierine and incipient chloritization in shallowly buried sandstone reservoirs: Key role of the source-to-sink context. *Geological Society of America Bulletin*, 2022, 134 (3-4), pp.739-761. 10.1130/B35865.1 . hal-03341574

HAL Id: hal-03341574

<https://hal.science/hal-03341574>

Submitted on 5 Aug 2023

HAL is a multi-disciplinary open access archive for the deposit and dissemination of scientific research documents, whether they are published or not. The documents may come from teaching and research institutions in France or abroad, or from public or private research centers.

L'archive ouverte pluridisciplinaire **HAL**, est destinée au dépôt et à la diffusion de documents scientifiques de niveau recherche, publiés ou non, émanant des établissements d'enseignement et de recherche français ou étrangers, des laboratoires publics ou privés.

**Authigenic berthierine and incipient chloritization in shallow-buried sandstone reservoirs:
key role of the source-to-sink context**

**Maxime Virolle¹, Benjamin Brigaud¹, Daniel Beaufort², Patricia Patrier², Eid Abdelrahman²,
Hadrien Thomas¹, Eric Portier³, Yann Samson⁴, Raphaël Bourillot⁵, Hugues Fénies⁵**

¹*Université Paris-Saclay, CNRS, GEOPS, 91405 Orsay, France*

²*Université de Poitiers, CNRS, UMR 7285 IC2MP, 6 rue M Brunet, TSA 51106, 86073 Poitiers
cedex 9, France*

³*CV Associés Engineering, 7 chemin de la Marouette, 64100 Bayonne, France*

⁴*Storengy, 12 rue Raoul Nordling, CS 7001, 92274 Bois-Colombes Cedex, France*

⁵*Géoressources et Environnement, ENSEGID, Bordeaux INP, Université Bordeaux Montaigne,
Pessac 33607, France*

Corresponding author: benjamin.brigaud@universite-paris-saclay.fr

ABSTRACT

Chlorite is recognized worldwide as a key mineral inhibiting the development of quartz cement in deeply buried sandstone reservoirs. Iron-rich chlorite is mainly formed by the transformation of a precursor clay mineral, however, few studies have focused on the early stages before the crystallization of chlorite. This study analyzed shallow-buried (400–1000 m) coastal sandstones from within the Wealden Group of the Paris Basin. Berthierine, a 7 Å trioctahedral clay mineral belonging to the serpentine group, approximatively with same chemistry as chlorite but a different crystal structure, has been identified in a 900 m deep well, but not in a 400–600 m deep well. Berthierine has mainly been observed as clay coatings around detrital grains, with a typical honeycomb texture. Nanopetrographic observations suggest that the honeycomb textural organization of the clay particles found in deeper buried sandstone reservoirs (>1500 m) is acquired from a berthierine precursor at

shallow depths. Although, small amounts of quartz overgrowths are observed on the surface of detrital grains at shallow depths and low temperature (below 40 °C), it is believed that precursor berthierine coatings are primarily responsible for the inhibition of quartz overgrowths before the formation of Fe-rich chlorite. This suggests that the key mineral primarily controlling the reservoir quality of deeply buried sandstone reservoirs is berthierine rather than iron-rich chlorite, challenging the commonly accepted assertion that chlorite coating is the main process that inhibits quartz overgrowths. The source-to-sink context of the Paris Basin during the Early Cretaceous was decisive with respect to the supply of sands and berthierine clay precursors (in particular kaolinite and iron-rich hydroxy-interlayered clay minerals) to the center of the Basin.

INTRODUCTION

Reservoirs located in estuarine formations include abundant chlorite coatings that contribute to the formation of complex heterogeneous reservoirs with moderate-to-excellent reservoir quality at burial depths of more than 2 km (Ehrenberg, 1993; Bloch et al., 2002; Worden and Morad, 2003; Dowey et al., 2012; Saiag et al., 2016; Worden et al., 2020). It has been demonstrated that authigenic chlorite enhances the reservoir quality in deeply buried sandstone reservoirs by inhibiting the development of quartz overgrowths (Pittman and Lumsden, 1968; Larese, et al., 1984; Dixon et al., 1989; Billault et al., 2003; Morad et al., 2010; Bahlis and De Ros, 2013; Bottig et al., 2017; Worden et al., 2020). Therefore Fe-chlorite crystals that occur as coats around detrital sand grains play a decisive part in the preservation of unusually high primary intergranular porosity in these reservoirs (Ehrenberg, 1993; Anjos et al., 2003; Worden et al., 2020). Laboratory experiments reproducing mineral nucleation show that Fe-rich chlorite can form from the transformation of precursor clay minerals, such as berthierine (an iron and aluminum-rich 7 Å trioctahedral clay mineral

belonging to the serpentine group), or odinite, or phyllite-V (Odin, 1988; Ehrenberg, 1993; Hornibrook and Longstaffe, 1996; Ryan and Reynolds, 1996; Aagaard et al., 2000; Ryan and Hillier, 2002; Morad et al., 2010; Beaufort et al., 2015; Haile et al., 2015). Chlorite grain coats have been reported from a wide range of depositional environments, but Fe-chlorite is most commonly found in coastal estuarine and deltaic environments (Dowey et al., 2012; Wooldridge et al., 2017; Griffiths et al., 2018a; Worden et al., 2020). Recent studies confirm that early clay coats form in modern estuarine environments are mainly composed of aggregates of detrital clays (illite, chlorite, kaolinite and sometimes dioctahedral smectite). So far, berthierine and odinite have not been observed, suggesting that they are not part of the initial sedimentary supply (Wooldridge et al., 2018; Griffiths et al., 2018a, 2018b, 2019; Virolle et al., 2019a).

Even if the chemical elements required for diagenetic Fe-chlorite crystallization did originate from the dissolution of the most reactive detrital minerals, it has been proposed that Fe-rich chlorite does not form directly from solutions by precipitation during eogenesis (Beaufort et al., 2015, and references therein). Instead, diagenetic chlorite is usually formed through complex chloritization processes that involve the formation of a precursor clay minerals (Odin and Matter, 1981; Ehrenberg, 1993; Morad et al., 2010; Worden et al., 2020). Aluminous silicates and iron-rich minerals of the serpentine group such as odinite and berthierine seem to be the primary precursor candidates (Odin, 1988; Ehrenberg, 1993; Hornibrook and Longstaffe, 1996; Ryan and Reynolds, 1996; Aagaard et al., 2000; Ryan and Hillier, 2002; Worden et al., 2020). It is believed that berthierine is either the product of direct neoformation or replacement during early diagenesis (Van Houten and Purucker, 1984) or that the green clay odinite evolves into berthierine during early diagenesis, producing the well-organized 7 Å structure (Odin, 1988; Hornibrook and Longstaffe, 1996).

73 With increasing burial depth, these precursors are believed to then be transformed into
74 chlorite via a mixed-layer mineral series under anoxic conditions (Hornibrook and Longstaffe,
75 1996; Beaufort et al., 2015; Worden et al., 2020).

76 Several authors suggested that the formation of Fe-chlorite occurrence in sandstones
77 requires sedimentary material that is essential for the formation of clay precursors such as
78 reactive aluminous silicates and iron-rich minerals (Morad et al., 2010; Gould et al., 2010;
79 Beaufort et al., 2015; Aja, 2019; Worden et al., 2020). Although green Fe-rich marine sands
80 composed of glauconitic minerals (Fe-bearing dioctahedral smectite, glauconitic smectite,
81 glauconitic mica), odinite and chamosite, an iron-rich 14 Å trioctahedral chlorite, are
82 relatively well-known (Porrenga, 1967; Van Houten and Purucker, 1984; Odin, 1988;
83 Hornibrook and Longstaffe, 1996) in both modern sediments and ancient sedimentary rocks,
84 there is a shortage of studies documenting both the conditions (depth, temperature) and
85 the timing of their formation throughout the shallow-burial history of the clastic sediments.
86 In addition, few of the studies document both the petrography and mineralogy of siliciclastic
87 sediments having undergone incipient chloritization at burial depths of 1000 m or more
88 (Hornibrook and Longstaffe, 1996; Tinseau, 2002). In particular, little is known of the origin
89 of berthierine in modern sediments.

90 Although the clays trapped in modern estuarine sands have been extensively studied in
91 recent years (Wooldridge et al., 2018; Griffiths et al., 2018b; Virolle et al., 2020; Worden et
92 al., 2020), there is a gap in the documentation of the suites of reactions that lead to the
93 transformation of detrital clays into chlorite precursors such as berthierine. Therefore, a
94 case study of shallow-buried clastic sediments in which berthierine has not started its
95 transformation into Fe-chlorite is critically needed to better understanding of the conditions
96 in which this clay mineral precursor forms and initiates chloritization (Hornibrook and

Longstaffe, 1996). Pisoids and pseudo-ooids composed of berthierine have been identified in outcrops of the Wealden Group sediments in South-East England (Taylor, 1990). In the Paris Basin (France) green clay minerals were reported in Wealden Group sandstones from core samples (Buissart et al., 1988). In the Paris Basin and in the Weald and Wessex Basins (UK), Lower Cretaceous Wealden Group sediments were mainly deposited in coastal settings, including fluvial, estuarine, deltaic and shoreface depositional environments (Allen, 1959; Buissart et al., 1988; Allen and Wimbledon, 1991; Thiry et al., 2006; Akinlotan, 2016, 2017). The Wealden Group sandstones of the Early Cretaceous period within the Paris Basin have not been well characterized in terms of sedimentology and mineralogy (Buissart et al., 1988).

The main goal of this paper is to provide petrographic and mineralogical analyses of green clay minerals in poorly consolidated Early Cretaceous sands having undergone shallow burial (depths less than 1000 m) during the geological evolution of the Paris Basin. These characterizations will be compared to the results of recent studies that reported detrital clay coats around sands in modern coastal environments (Wooldridge et al., 2018; Griffiths et al., 2018a; Virolle et al., 2019b; Worden et al., 2020; Duteil et al., 2020). The Wealden sediments will be used as an analogue for the eogenetic processes that modern sands undergo. Five wells from the Wealden Group sandstones of the Paris Basin with burial depths ranging from 400 to 1000 m, have been selected to address the following specific questions relating to sedimentology of the Wealden Group sandstones and to early clay diagenesis in sandstones:

1. Do Wealden Group sandstones allow better characterisation of the intermediate diagenetic stage between the formation of detrital clay coats and the crystallization of true Fe-rich chlorite in sandstone reservoirs?

2. What are the facies and depositional environments of the Wealden Group sandstones of the Paris Basin?
3. What are the clay mineral assemblages of the Wealden Group sandstones of the Paris Basin?
4. Are incipient quartz overgrowths present within this reservoir?
5. Does incipient pre-chloritization processes already limit the development of early quartz overgrowths?
6. What are the detrital clay minerals that are precursors to chloritization?
7. What is the source to sink context suitable for chloritization?

GEOLOGICAL SETTING

The Paris Basin is located in northern France and forms an intracratonic basin about 600 km in diameter. The maximum burial depth reaches about 3200 m in the central basin (Fig. 1A-B, Guillocheau et al., 2000; Gély and Hanot, 2014). The basement of the Paris Basin is composed of Hercynian and Cadomian crystalline rocks covered by a series of sedimentary deposits laid down from the Triassic to the Miocene (Guillocheau et al., 2000; Fig. 1A-B, Gély and Hanot, 2014). This basin is surrounded by four Palaeozoic Massifs: the Armorican Massif to the west, the Central Massif to the south, the Vosges to the east and the Ardennes to the north. In its north-western part, the basin extends from the English Channel to the Wessex and Weald Basins in England. Basin structures and sedimentary formations are very similar on both sides of the English Channel.

Tectonic activity in the Paris Basin ceased at the beginning of the Miocene (Bergerat et al., 2007). From the Early Jurassic to the Oligocene, sediments were deposited in a marine environment, periodically coastal or lacustrine, in a series of transgressive and regressive episodes. Since the Triassic period, the depositional environments have produced a multi-

144 layered aquifer system made up of alternating permeable layers, dominated by either
145 lithified or poorly consolidated limestones and sandstones, and less permeable layers
146 consisting mainly of marls and clays (Fig. 1A, Mégnien and Mégnien, 1980). During the Early
147 Cretaceous, geological structures of the Paris Basin were controlled by the progressive
148 opening of the North Atlantic Ocean and by the earliest effects of the convergence between
149 the Eurasian and African plates (Guillocheau et al., 2000). During the Early Cretaceous,
150 sedimentation was marked in the Weald, Wessex and Paris basins by coastal, estuarine to
151 fluvial deposits (Fig. 1C, Dercourt et al., 2000). Palaeogeographic reconstructions show that
152 the north-eastern Paris Basin was located at tropical to subtropical latitudes during the Late
153 Jurassic–Early Cretaceous (28–35°N, Dercourt et al., 2000). In England, Wealden Group
154 sediments can reach a thickness of about 800–900 m as on the Isle of Wight (Allen, 1959).
155 The thickness of the Wealden Group sandstones appears to be considerably reduced in the
156 central part of the Paris Basin where it never exceeds 200 m (Buissart et al., 1988).
157 Corresponding deposits on the north-eastern edges of the Paris Basin are absent (Thiry et
158 al., 2006). The deposition area during the Early Cretaceous was reduced to a NW–SE oriented
159 trough connected to the Tethys sea (Fig. 1C, Buissart et al., 1988; Thiry et al., 2006). During
160 the Early Cretaceous, the Wealden trough extended from the Land of Bray, west of Beauvais,
161 to Burgundy, region around Dijon (Thiry et al., 2006). Jurassic formations cropped out on
162 both sides of the gutter and were submitted to weathering based on the presence of lateritic
163 soils (Thiry et al., 2006). Alternating transgressive/regressive periods influenced the Wealden
164 Group sands that are either (1) continental or (2) marine shallow-marine to coastal (Mégnien
165 and Mégnien, 1980; Rusciadelli, 1996). Wealden Group sandstones represent several
166 second-order transgressive/regressive sequences (Rusciadelli, 1996). Up to six second-order
167 transgressive/regressive facies cycles have been identified within the overall first-order Early

Cretaceous transgressive phase (Jacquin et al., 1998). The top of Wealden Group sandstones is capped by a low permeability layer known as the Aptian shale (Jacquin et al., 1998). The Lower Cretaceous Wealden Group sandstones of the Paris Basin forms a strategic reservoir unit, supplying drinking water for Paris. At depths greater than 500–600 m, this formation is also a potential target for the future development of deep geothermal energy around Paris (Bel et al., 2012). Away from Paris, the Wealden Group sandstones are used for gas storage (Mégnyen and Mégnyen, 1980; Buissart et al., 1988; Vernoux et al., 1997; Bel et al., 2012; Seguin et al., 2015). This interval is generally referred to as the Neocomian reservoir in geochemical or hydrological studies of the Paris Basin (Castro et al., 1998). The reservoir units range from Berriasian to Barremian in age, or to the first Aptian–Albian marine layers in the Paris Basin (145 Ma to 195 Ma; Mégnyen and Mégnyen, 1980). Neocomian reservoirs are valuable aquifers for geothermal use in the Paris Basin. Previous studies have indicated current water temperatures of 32 °C at 744 m at Ivry-sur-Seine, in the South-Eastern suburbs of Paris (thermal gradient of 2.6 °C/100 m, Seguin et al., 2015) and 34 °C at 740 m at Bruyère-le-Chatel, located 30 km South-Western of Paris (thermal gradient of 3.9°C/100m, Le Nir et al., 2009).

MATERIAL AND METHODS

The Wealden Group core samples studied in this report consist of sandstones from three geographical sites in the Paris Basin: (1) Fouilleuse, (2) Beynes and (3) Crouy-sur-Ourcq (Fig. 1A). Fouilleuse is located 10 km west of the Gournay-sur-Aronde underground gas storage site and about 60 km NNE of Paris in Wealden Group sandstones. Two wells (FO-01 and FO-06) from the Fouilleuse site were studied. Borehole FO-01 was drilled close to Avrechy (Oise), and borehole FO-06 was drilled in 1994 close to Saint-Rémy-en-l'éau (Oise), 1.5 km north-east of borehole FO-01. The studied sandstones are located at a depth of 445–510 m

192 in borehole FO-01 and 477–530 m in borehole FO-06. Two wells (A and B) were drilled in the
193 Beynes gas storage site (Yvelines), 35 km west of Paris, which has been exploited since 1956.
194 Sandstones were sampled at 390–430 m depth for well A and at 420–440 m depth for well B.
195 Lastly, well CR12 was drilled near Crouy-sur-Ourcq on the Germigny-sur-Coulombs
196 underground gas storage site, 60 km NE of Paris, at a depth of 900–970 m. The maximum
197 burial depths of Wealden Group sandstones range from 440 m at Beynes to 1000 m at
198 Crouy-sur-Ourcq. The present day temperature in well CR12 at a depth of 897 m is 36 °C
199 yielding a thermal gradient of 2.6 °C/100 m. The presence of Upper Cretaceous and
200 Palaeogene sediments suggests that the present-day temperature corresponds to the
201 maximum burial temperature attained and maintained during the last 40 million years of the
202 basin's history (Fig. 2, Torelli et al., 2020).

203 Some 250 m of cores from the five different wells were logged to determine the lithology,
204 the vertical facies associations, and 60 rock fragment or plug samples were collected.
205 Mineralogical analyses were made on all samples. Forty-seven thin sections were made for
206 detailed petrographic observations.

207 Petrographic studies were carried out on thin sections and rock fragments using a polarizing
208 optical microscope (Nikon Eclipse E600POL) and a scanning electron microscope (SEM) JEOL
209 IT 500 equipped with an Bruker Energy Dispersive X-ray Spectrometer (EDS) using an XFlash
210 4030 Silicon drift detector. SEM observations were performed in secondary electron imaging
211 (SEI) mode for morphological documentation and backscattered electron (BSE) mode on
212 carbon-coated thin sections for the imaging of chemical contrast and selection of local sites
213 for sporadic chemical analysis. Analytical conditions were 15 kV, 1 nA, a counting time of
214 50 sec, and at a working distance of 11 mm. The standards used for EDS consisted of albite
215 (Na, Al, Si), almandine (Mg, Fe), diopside (Ca), orthoclase (K) and spessartite (Mn). Matrix

216 corrections were performed using the integrated programme (PhiRhoZ correction). The
217 reproducibility of the standard analyses was nearly 1.5% for all of the elements, except Na,
218 which attained a reproducibility of 3%.

219 Focused Ion Beam ultra-thin sections were made at the CINaM centre (Université Aix
220 Marseille, France). This nanofabrication station contains an FEI Helios 600 nanolab SEM
221 coupled to a focused Ga⁺ ion beam (FIB) column. The sections obtained were about 10 µm x
222 8 µm x 50 nm in size.

223 The relative surface area (%) of the macropores and the solid components (coated and non-
224 coated quartz, feldspars, lithics, micas, bioclasts, pyrite, iron-rich carbonates, diagenetic
225 cements, clay matrix) were quantified from thin sections using the JmicroVision Image
226 analysis software employing random grid point counting (Roduit, 2007). A minimum of 800
227 counts was performed on 20 different images (2.5 mm x 2.5 mm) in each thin-section.

228 The chemical compositions of clay minerals derived from EDS analyses were expressed in
229 oxide weight percentages, atomic percentages were used to calculate structural formulas on
230 the basis of the stoichiometric number of oxygen. Atomic concentrations were plotted in
231 ternary diagrams of $MR^{3+}-2R^{3+}-3R^{2+}$ (Velde, 1985) to determine the compositional field of
232 clay minerals and to highlight mixtures at the micrometre scale from the point count
233 analysis.

234 X-Ray Diffraction (XRD) analyses of randomly oriented powders were acquired to determine
235 the bulk mineralogy of each sample using a PANalytical X'Pert diffractometer. X-ray
236 diffractograms of randomly oriented powders were acquired between 4° and 80° 2θ with a
237 step size of 0.017° 2θ, a time/step of 3s using CuKα X-ray radiation at 45 kV, 40 mA with a
238 0.0170 step size. A routine XRD analysis on the fraction less than 2 µm was acquired at the
239 Géosciences Paris-Saclay laboratory (Université Paris-Saclay, France) using a PANalytical

240 X'Pert Prodiffractometer using CuK α 1 with a 0.0170 step size between 3° and 35° 2 θ at 45 kV
241 and 40 mA. Semi-quantitative estimations of kaolinite, chlorite, illite/micas and smectite
242 were realized with MacDiff software (Goethe Universität) based on the peak area of the
243 ethylene–glycol diffractograms summed to 100%, the relative error for the peak area being
244 $\pm 5\%$. A second set of detailed diffraction patterns of oriented and randomly oriented
245 preparations of the clay size fraction (less than 2 μm and less than 0.2 μm) was acquired at
246 the Institut de Chimie des Milieux et Matériaux de Poitiers (IC2MP) laboratory (Université de
247 Poitiers, France) using a Bruker D8 XRD diffractometer (CuK α radiation) equipped with a
248 linxeye detector. The XRD patterns of randomly oriented powders were recorded over the
249 range of 2–65° 2 θ with 0.02° 2 θ steps and 5 seconds per step. XRD patterns of oriented
250 preparations were recorded over the 2–30° 2 θ range with 0.02° 2 θ steps and 1 second per
251 step.

252 Due to their poorly consolidated nature, sandstone samples were gently disaggregated in
253 water and the clay fraction put in suspension by ultrasonic treatment without grinding. Clay
254 size fractions <2 μm and <0.2 μm were extracted by sedimentation and centrifugation,
255 respectively. No cation exchange was performed on the clay material. Particles less than
256 0.2 μm in size were extracted from the infra 2 μm clay suspension by using a Beckman J2-21
257 continuous centrifuge rotating at 5000 rotations per minute with a constant flux of the
258 suspension passing through the rotor set at 150 ml per minute.

259 XRD patterns of mixed-layer minerals have been interpreted on the basis of comparison with
260 one-dimensional diffraction profiles calculated using Newmod 2TM software.

261 Fourier Transform Infrared Spectroscopy (FTIR) was obtained from the less than 2 μm
262 fraction, only from samples in which X-ray diffraction indicated the presence of berthierine.

263 The mid-infrared (MIR) spectra (400–4000 cm^{-1}) were acquired on KBr pellets using a Nicolet

760 FTIR spectrometer equipped with a potassium bromide (KBr) beamsplitter and a DTGS-KBr detector. The resolution was set to 4 cm^{-1} with a co-addition of 100 scans. KBr pellets were made with 1 mg of clay material dispersed in 150 mg of KBr powder and pressed under 8 tons for 5 minutes in a hydraulic press before being dried for 12 hours at $200\text{ }^{\circ}\text{C}$. Heating to $200\text{ }^{\circ}\text{C}$ was used to remove the OH bending and stretching bands of adsorbed water (weakly bonded OH) which absorb IR radiation in the same range of frequencies as the OH stretching bands of berthierine (near 3400 cm^{-1}). Details of location, petrographical and clay mineral compositions by sample are provided in Supplemental Material¹ Table S1 (sample description).

RESULTS

Sedimentary Facies

From the core descriptions, we identified the depositional environments as ranging from the most distal (offshore) to the most proximal (alluvial plain) environments. We grouped the facies into five facies associations, typical of five depositional environments (Fig. 3, Table 1). Observations and descriptions are summarized in Table 1. Well CR12 shows the variability in the sedimentary environments identified within the Wealden Group sandstones of the Paris Basin (Fig. 3).

The first facies association (FA1) consists of fluvial deposits, such as trough cross-bedded sandstones (which can be locally conglomeratic) with numerous soft mud pebbles, current-rippled sandstones, nodular siltstones, laminated siltstones, dark rooted silty mudstones, and coal beds (Fig. 3, Fig. 4A-B). This facies association exhibits an overall fining-upward succession ranging from medium to upper fine-grained trough cross-beds to fine-grained ripple-laminated sandstones. Continental conditions are highlighted by the absence of

marine microfossils, the abundance of continental organic material (wood fragments, leaf debris), and the relative abundance of the fresh-water algae *Botryococcus spp.*, or continental spores *Densoisporites spp.* as reported by Rusciadelli (1996).

The second facies association (FA2) is estuarine (Fig. 4C-G) and is similar to the well-characterized vertical facies association described on cores from the modern Gironde estuary. FA2 appears to be a mixed environment, with some continental indicators, an assemblage of pollens and spores, such as *Classopolis spp.* or *Exesipollenites spp.* (Rusciadelli, 1996), and some marine indicators, *Muderongia crucis*, *Stiphrosphaeridium anthophorum* and dinoflagellate *Rhynchodiniopsis fimbriat*. This facies association is key to understanding the development of early clay grain coats. Three facies make up this facies association:

(1) The first facies (FA2a) consists of medium- to fine-grained sandstones with trough cross-stratifications, separated by thin clay layers. Foresets are highlighted by clay drapes and organic matter (Fig. 4C). Reactivation surfaces are also visible. Compositionally, FA2a consists of angular to sub-rounded, quartz grains, feldspar and mica, with rare glauconite ooids. Foresets with clay drapes, trough cross-stratifications, reactivation surfaces and a mix between continental and marine pollens and spores are consistent with small sandy tidal dunes, deposited in subtidal or intertidal zones, forming tidal bar deposits in an estuary.

(2) Facies FA2b is characterized by three types of fine bedding that are vertically stacked: (i) flaser bedding composed of medium-grained, current-rippled sands with muddy couplets (Fig. 4D-E); (ii) wavy bedding, with alternating millimetre-to-centimetre, fine-grained sandy ripples and amalgamated levels of tidal slack water clay drapes (Fig. 4F), and (iii) fine-grained, lenticular to wavy bedding sandy ripples, with alternating millimeter-scale silty linsens and high-tide slack water clay and clay drapes (Fig. 4G). Rare bioturbation fabrics are

observed, composed mainly of *planolites*. The variable bedding types and the mix between continental and marine pollens and spores suggests tidal flat deposits.

(3) The third facies (FA2c) is composed of amalgamated clay drapes, rich in organic matter, with localised reed roots and oxidized pedogenic horizons. The presence of roots, organic matter and oxidized pedogenic horizons suggests supratidal marsh facies covering the tidal flat of an estuarine alluvial plain.

The FA2 association, as a whole, may be interpreted as ranging from fining upward, tidal bar and tidal channel deposits to prograding estuarine alluvial plain deposits.

The deltaic facies association (FA3) consists of cross-bedded sandstones overlain by shales and limestones with fragments of marine bivalves, echinoderms and brachiopods. Vertical tubes of *Skolithos linearis*, *planolithes* or *teichichnus* are present (Fig. 4H) and marine microfossils, such as the dinoflagellate *Muderongia crasis* or *Oligosphaeridium asterigerum* (Rusciadelli, 1996) are also present.

FA4 is interpreted as a shoreface facies association. It is mainly composed by fine- to medium-grained, clean, well-sorted sandstones in 20 cm to 1 m thick beds, with hummocky, swaley, low-angle to horizontal planar cross-stratifications which are locally scrambled and heavily bioturbated (Fig. 4I). Locally, vertical burrows (*skolithos*) are present, as well as variably abundant *ophiomorpha* burrows in the coarser sands. Dispersed marine shell fragments and local accumulations of shells are also present in the upper section (Fig. 3).

FA5 consists of shale, with thin horizontal laminae of siltstone, which commonly contains a mixture of bivalves, coccoliths, foraminifera and scattered shell fragments. This is interpreted as an offshore facies association.

The vertical stacking pattern is complex, with the presence of numerous erosion/reactivation surfaces suggesting relatively limited accommodation space.

336

337 **Mineralogy of Pre-Burial Sediments (Early Cretaceous, Surface Sediments)**

338 ***Grain Composition and Grain Coating***

339 Sandstones of the Wealden Group sandstones of the Paris Basin are mainly composed of
340 quartz (34% on average) and feldspars (5% on average) associated with lithics such as Fe
341 ooids or mud clasts (9% on average), (Fig. 6E, 6G-H), and micas (Fig. 5, Table 2). Iron-ooids
342 are present in some samples (Fig. 6E, G-H). XRD and SEM/EDS analyses indicate that these
343 ooids are composed of goethite, an iron hydroxide mineral, which crystallized around a
344 quartz sand nucleus (Fig. 6H). Locally, these iron-coated grains can be abundant, forming
345 green sands (Fig. 6E). Grain size varies from well to well, but mostly consists of fine to
346 medium grained sub-rounded to sub-angular, moderately well sorted sandstones which are
347 mostly classified as feldspathic litharenite (Folk Classification, Folk, 1974). Minor amounts of
348 lithic arkose, litharenite or sublitharenite were also identified (Fig. 5, Table 2).

349 Many of the sand grains are coated by fine grained material (Fig. 6A-D) composed of clay,
350 silt, and very fine grained non-clay silicates, such as coccoliths (Fig. 6B-F). The clay coats form
351 bridges (Fig. 6A), aggregates (Fig. 6C), ridges (Fig. 6D), or clay drapes around and between
352 quartz grains that are very similar to textures observed in modern estuaries (Wooldridge et
353 al., 2017; Virolle et al., 2019a) (Fig. 6).

354 All facies association are coated with variable amounts of detrital clay (Fig. 7), Fluvial facies
355 association = 37%; Estuarine facies association = 39%; Deltaic facies association = 5%;
356 Shoreface facies association = 12%; and in the Offshore facies association = 2% (Fig. 7, Table
357 2). In addition, detrital grain coats are present in all wells (Supplemental Material¹ Table S1).
358 In fluvial and estuarine facies associations, detrital coats cover 15–30% of the surface of
359 sand grains (Fig. 7, Table 2). However, all facies combined, well CR12 also has a lowest clay

fraction (6 wt% on average) compared to 10 and 23 wt% in the Fouilleuse and Beynes wells respectively (Supplemental Material¹ Table S1).

Clay Minerals

XRD analyses of the less than 2 μm clay fraction reveals a clay mineral assemblage that is composed mainly of kaolinite (42% on average, based on peak areas), chlorite (22% on average), illite/micas (26% on average) and smectite (11% on average); (Fig. 3 and Table 2). This detrital clay mineral assemblage was observed in all wells (Fig. 3 and Supplemental Material¹ Table S1).

XRD patterns obtained from oriented preparations of less than 2 μm particles of the clay coats are reported in Figure 8. They highlight a much more complex mineralogical composition than obtained from the preliminary routine XRD analysis which considered only mixtures of discrete kaolinite, illite/mica (named illite hereafter for simplicity), chlorite and smectite (Fig. 3).

Discrete illite and kaolinite are identified by the presence of rational 00ℓ reflections at 9.99 Å, 4.98 Å and 3.33 Å and at 7.14 Å and 3.57 Å respectively, after air drying and ethylene glycol treatments. In all investigated samples, the diffraction maximum at 14.3 Å observed in air drying state, does not fit with the d_{001} reflection of chlorite due to the lack of rational subordinate reflections and by a partial but limited shift towards lower angle positions (up to 16.3 Å, Fig. 8A) in the ethylene glycol state, which is inconsistent with that of smectite in most samples. Such behaviour is typical of iron-rich hydroxy-interlayered clay minerals (HIM) that commonly occur in acidic soil environments and contain Al and Fe cations (Barnhisel and Bertsch, 1989; Meunier et al., 2007; Lanson et al., 2015). In those studies, XRD profiling suggests that hydroxy-interlayered clay minerals (HIM) consist of no less than 10

mineralogical clay phases (Viennet et al., 2015, 2016). Barnhisel and Bertsch (1989) reported that hydroxy-interlayered smectite (HIS) and hydroxy-interlayered vermiculite (HIV) are intermediate mineral phases of the solid-solution series between fully expandable dioctahedral 2:1 phyllosilicates (smectite) and pure Al-chlorite (dombassite). These clays are believed to form during the weathering process in acidic soils which results in the interlayer Al-hydroxylation and Fe-hydroxylation of 2:1 phyllosilicates (Carstea, 1968).

The XRD patterns of the clay material which partially coats the sand grains are analogous to those reported by Viennet et al., (2015) for the temperate acidic soils in a forest. On the low angle side (i.e. between 10 and 17 Å) the XRD patterns obtained after air drying and ethylene glycol treatment are complex:

(1) In a few samples, the peak shifting toward lower angles after ethylene glycol treatment does not reach the 17 Å d-spacing value of the d_{001} of smectite (Fig. 8A). This observed d-value near 16 Å (Fig. 8E) is attributed to the presence of a HIS clay phase (Barnhisel and Bertsch, 1989; Meunier et al., 2007); (2) There is a very limited shift of the 14.3 Å peak after EG treatment (Fig. 8B, C, D,) which is attributed to the presence of the HIV phase (Barnhisel and Bertsch, 1989; Meunier et al., 2007). This could correspond to the presence of a dioctahedral chlorite-like clay phase which represents the final stage of complete Al-hydroxylation of the interlayer sheet of HIMs and/or to the presence of a very small amount of detrital chlorite (Chlorite has been identified from SEM observations in a few samples); and (3) a very broad diffraction peak (or shoulder) with maxima near 12 Å in the XRD pattern of the air dried assay (Fig. 8B, C, D) and with a limited shift toward lower angles after ethylene glycol treatment. Such positions have been interpreted as due to the presence of mixed layer minerals (MLM) composed of illite and hydroxyl-interlayered layers, with most likely minor amounts of smectite (Viennet et al., 2015, and references therein).

On the high angle side, the broad peaks observed near 7.7 Å, 4.80 Å and 3.50 Å are consistent with the presence of MLM composed of expandable HIMs, especially HIS and non-expandable HIMs with a di-dioctahedral chlorite structure (i.e. dombassite-like clay phase).

Moreover, comparison between the XRD patterns of clay particles from different grain sizes populations (Fig. 8C-8D) shows that the amount of discrete illite and kaolinite falls markedly (in FO6-12 sample, fraction lower than 0.2 µm), having been replaced by HIMs and complex mixed-layer minerals (MLMs) in the smaller clay fraction (less than 0.2 µm, Fig. 8D).

The chemical compositions representative of clay particles from pre-burial clay-coats (before burial, at the surface) are presented in Table 3 (analyses 1 to 4). Chemically, the pre-burial clay coats are characterized by a large range of high Al₂O₃ content (from 21 to 37%) and moderate to high iron content expressed as Fe₂O₃ content depending on their weathering origin (3–15%). When plotted in the MR³⁺- 2R³⁺-3R²⁺ ternary diagram (Velde, 1985), the point chemical analyses of detrital clay coats fit within an overall compositional field of dioctahedral phyllosilicates which extends over the fields for illite, dioctahedral smectites, and kaolinite/dombassite (Fig. 9A). Such a compositional field is consistent with the aforementioned XRD identification of pre-burial clay minerals. When plotted in an Fe-Al-Mg ternary diagram (Fig. 9B), the compositional field of pre-burial clays spreads over a large range of Fe content which varies with the relative amounts of soil kaolinite (3–4% Fe₂O₃) and HIMs (up to 15% Fe₂O₃) in the analysed particles.

SEM/EDS analyses indicate that green clay minerals forming sand grains are composed of Fe-rich chlorite detrital grains observed in a few samples only (such as FO6-17). Although clay minerals of pedogenic origin have been identified in each well, their relative proportion seems to vary with their sedimentology. Discrete kaolinite is dominant in the sandy facies of

the estuarine environment while HIMs and associated MLMs are dominant in sandy/muddy facies of the estuarine environment.

Authigenic Minerals

Based on petrographic observations, we recognize two primary diagenetic stages which were characterized by cementation, dissolution and recrystallization.

The first stage consists in the crystallization of authigenic pyrite, siderite, ankerite and vermicular kaolinite. We identify kaolinite in all the wells studied, regardless of sample burial depth.

Pyrite is commonly observed within the detrital clay coats and exhibits a typical framboidal texture. It is composed of spherical aggregates of pyrite octahedrons (0.5–2 μm in diameter) which are frequently embedded in the clay material (Fig. 10A, 10F and 10J). Framboidal pyrite is very common in reducing marine sediments and has been interpreted to be the result of pyritization associated with the decay of organic matter mediated by bacteria during the first stage of diagenesis (McKay and Longstaffe, 2003). Blocky crystals of pyrite are relatively rare in these sediments (Fig. 10B).

Fe-rich carbonates occur as euhedral crystals, forming a discontinuous coating on the surface of the framework silicates (Fig. 10C-I). They are believed to have formed as a primary cementation stage during the early diagenesis of the sandstones.

Siderite (Fig. 10C-F) and ankerite (Fig. 10G-I) occur as equant or elongate rhombic crystals with a mean size ranging from 10 to 100 μm (Fig. 10C-F) and show evidence of chemical zoning (Fig. 10E-F). Siderite is typically associated with the pyrite crystals (Fig. 10F).

SEM observations revealed that the initial clay formation consisted of the precipitation of stacks of relatively coarse-grained pseudo-hexagonal (about 10 μm in diameter) of

vermicular kaolinite on detrital clay coats in the open pore space (Fig. 11A-B). FTIR spectra of the clay material in the hydroxyl-stretching band region of phyllosilicates reveals the four diagnostic bands of kaolinite (i.e., 3695, 3668, 3652 and 3620 cm^{-1}) in all studied wells and indicates the presence of two types of kaolinite with specific crystal-chemical properties (Fig. 11C). In the shallower samples, poorly crystallized kaolinite of detrital origin (characterized by a weak and broad band reflection at 3668 cm^{-1} and a band at 3598 cm^{-1} which is indicative of vibration of the $\text{AlFe}^{3+}\text{-OH}$ bond (Delineau, 1994)), is particularly abundant. In contrast, deeper samples (CR-12, Fig. 11C) are characterized by well-crystallized kaolinite with sharp diagnostic bands and the absence of the $\text{AlFe}^{3+}\text{-OH}$ bands. This suggests that during the shallow burial history of these sandstones, iron-rich and poorly crystallized kaolinites in the detrital clay matrix, underwent recrystallization resulting in the formation of well-crystallized vermicular kaolinite, similar to what has been described by Beaufort et al., (1998).

The second stage consists of the crystallization of a thin clay coat composed of tiny flakes of Fe-rich clay minerals which covers both detrital and authigenic minerals during the first stage of diagenesis. These diagenetic clay coats are continuous at the scale of SEM observations and have only been observed in sandstones buried at depths exceeding 900 m (well CR12). SEM observations document the presence of honeycomb, Fe-rich clay coats covering the entire surface of the pre-existing minerals (Fig. 12A, 12B). Detailed SEM observations of ultra-thin FIB sections cut perpendicularly to the contact between detrital quartz and authigenic Fe-rich clay coats (Fig. 12C) reveal small (less than 100 nm) quartz overgrowths on the detrital quartz grains. These incipient quartz overgrowths are limited to the interstices between the Fe-rich clay crystallites and the detrital quartz grain surface. This nanopetrographic observation is very similar to that documented from TEM investigations at

the interface between detrital quartz and Fe-chlorite coats in several sandstone reservoirs (Billault et al., 2003). Moreover, the vermicular kaolinites which formed during the first diagenetic stage, show irregular, rounded shapes with eroded edges, suggesting partial dissolution, when the kaolinite was in contact with the iron-rich clay particles (Fig. 12B).

The Fe-rich clay minerals, which comprise the diagenetic Fe-rich clay coats, have been identified as berthierine on the basis of XRD, TEM and FTIR results. Berthierine is difficult to identify from XRD patterns of oriented preparation of the clay fraction because of its intense 00 ℓ reflections which is similar to kaolinite (Fig. 13). The Fe-rich clay coating identified by SEM/EDS and from the XRD patterns of randomly oriented powder preparations (Fig. 14A) as berthierine, has only been identified in samples buried at depth exceeding 900 m (Figs. 9 and 12). These XRD patterns differ from those of shallow buried samples (depth less than 500m, Fig. 14) in that they contain all of the peaks corresponding to the diagnostic hk reflections of berthierine, as referenced in literature (Brindley and Brown, 1980). More particularly, berthierine is unambiguously indicated from a series of peaks, marked by an asterisk in Figure 14A (d-spacing = 4.67 Å, 2.68 Å, 1.56 Å and 1.52 Å respectively). These peaks are not overlapped by the peaks of kaolinite or any other 2:1 dioctahedral phyllosilicates, such as HIMs or illite (Fig. 14A). In addition, the 060 reflection close to 1.56 Å (Fig. 14B) is indicative of a *b* parameter (*b*=9.36 Å) which is similar to that given in literature for berthierine (Brindley and Brown 1980). From the XRD results, it appears that the increasing amount of berthierine, in the clay fraction of samples buried at depth exceeding 900 m, is coupled with a marked decrease in the amount of detrital kaolinite and HIMs (Fig 14B). No diffraction peaks of chlorite can be identified in the XRD patterns of samples containing berthierine. The broad bands near 3550 and 3400 cm⁻¹ observed in the FTIR spectra on dehydrated samples of sandstones in which diagenetic clay coats were observed

(Fig. 15) are also key diagnostic features for the identification of natural or synthetic berthierine minerals (Mackenzie and Berezowski, 1984; Rivard et al., 2013 and references herein).

When plotted in the $MR^{3+}-2R^{3+}-3R^{2+}$ and Al-Fe-Mg ternary diagram, the EDS analyses of the diagenetic clay coats spread over compositional fields (Fig. 10A and 10B) which extend between that determined in the pre-burial clays and that of berthierine as determined from data in the literature (Bhattacharyya, 1983 and references herein). More particularly, the chemical composition of the iron-rich particles is very similar to that of berthierine as determined in the Wealden Group sediments in South-East England (Taylor, 1990). Such an overall compositional field suggests that, in many cases, admixture with, or juxtaposition to, berthierine of very fine particles of pre-burial clay minerals (illite, smectite, kaolinite, HIMs, etc.) still persists in the diagenetic clay coat. Locally, the last diagenetic phase is marked by blocky calcite cement filling the residual intergranular space.

DISCUSSION

Paragenetic Sequence Of The Wealden Group Sandstones

From the petrographic observations, we specify the timing of the diagenetic events (Fig. 16). This paragenetic sequence was established by cross-referencing and superimposing textural features observed using the optical microscope and SEM (Figs. 10, 12 and 16).

First, detrital clay coats form around sand grains at the time of sedimentation. The mineralogy of these detrital clay coats consists of variable quantities of kaolinite, illite, smectite and HIMs, the relative proportions of which vary depending on the original depositional setting (Table 1). Detrital clay coats consist of various textures, such as bridged

or ridged clay coats. The percentage of grains with detrital clay coats ranged from 37% in fluvial facies (Table 1) and 39% in estuarine facies (Table 1) which is far higher than the 20% reported from the modern tidal bars of the Gironde estuary, but similar to values reported in the estuarine point bars of the Garonne (Virolle et al., 2019a, 2020). Coat coverage is also similar to the alluvial part of the Ravenglass estuary (U.K.), where the majority of the sand grains are covered by approximately 30% clay coats (Griffiths et al., 2018a, 2019). Fe-ooids are found in wells FO-01 and FO-06 in the deltaic facies (FA3), but also in well, CR12. XRD, SEM/EDS and IR indicates that Fe-ooids consist of goethite (Fig. 6H, Fig. 13, Fig. 14 and Fig. 15), similar to what has been reported in the Wealden Group sandstones of the Eastern Paris Basin (Brigaud et al., 2018). Considering all facies, the coated grain content is on average higher in the deeper well (CR12, 41%) than in the shallow boreholes (Beynes and Fouilleuse with: 23% and 28% respectively).

During the first stage of diagenesis (eodiagenesis), framboidal pyrite (<20 μm) form in the detrital clay coats, probably in response to the reducing conditions imposed on the marine sediments during the decay of organic matter (McKay and Longstaffe, 2003).

The next event, early in the burial history (at a depth of about 500 m), includes kaolinite recrystallization through a dissolution-crystallization mechanism which gradually improvement its crystallinity (Fig. 11). At much the same time, siderite and ankerite formed as they are also observed coating grains, including around Fe-ooids that later partly dissolved (Fig. 10C-I). At greater depth, only within the deepest well CR12, some minerals were partially dissolved, including the iron ooids (goethite), kaolinite, and detrital micas (Fig. 10B-C). Authigenic berthierine crystallized forming a thin and continuous clay coat on both detrital and earlier eogenetic minerals (Fig. 12). The coat morphology also changed with

550 burial depth, from partial coats (ridges, bridges) to more complete berthierine coats around
551 the sand grains (Fig. 12). Berthierine coats completely cover grain surfaces, including
552 eogenetic pyrite and some incipient low temperature quartz overgrowth (Fig. 12). The
553 growth of quartz was stopped by the formation of the berthierine grain coats (Fig. 12C).
554 Ankerite coatings coexisted with the berthierine, suggesting that iron played a key role in the
555 paragenesis. At even greater depths, within the deepest well (CR12), blocky calcite cement
556 formed partially filling available intergranular pore space.

557 It is believed that the precipitation of berthierine is the first step before the chloritization
558 and that early berthierine clay coats are the precursor mineral for the iron-rich chlorite,
559 frequently observed in deeper buried sandstone reservoirs around the world (Morad et al.,
560 2010; Worden et al., 2020). In our study, it is believed that the berthierine observed at a
561 burial depth of about 900 m, marks the initiation of chloritization.

562 Quartz overgrowths and authigenic berthierine clay coats formed on the surface of detrital
563 grains of poorly consolidated sandstones buried at depths of less than 1 km. These two
564 minerals are cogenetic but growth of secondary quartz in the pore space appears to have
565 been prevented by the formation of berthierine crystallites at the base of the diagenetic clay
566 coat. This means that, in the Wealden Group sandstones case study, the inhibition of quartz
567 cementation in pore spaces of sandstones, which is of major importance for the
568 preservation of good reservoir quality, was initiated before and not after the conversion of
569 berthierine to Fe-chlorite, as usually considered in the literature (Pittman and Lumsden,
570 1968; Larese, et al., 1984; Ehrenberg, 1993; Bloch et al., 2002; Beaufort et al., 2015; Saiag et
571 al., 2016; Worden et al., 2020). In the 1990's, works on temperature and kinetics of quartz
572 growth suggested that most quartz cement precipitates at temperature higher than 80 °C

(Walderhaug, 1994b, 1994a, 1996; Lander and Walderhaug, 1999; Walderhaug et al., 2000; Lander et al., 2008) This minimum temperature of 80 °C was partly suggested because quartz cements were infrequently observed in sandstones that have never been buried at temperatures greater than 70-80 °C, and also because fluid inclusions in quartz overgrowths rarely reveal homogenization temperatures below 70-80 °C (Walderhaug, 1994b, 1994a). In this study, we have shown that small quantities of quartz overgrowths, formed on the surface of detrital quartz grains at depths of less than 1 km and temperature below 40 °C. These secondary quartz overgrowths are cogenetic with berthierine minerals, but growth of quartz was inhibited by the formation of early berthierine clay coats. Thus, this diagenetic study of the Wealden Group sandstones provides proof that minor amounts of quartz cement does precipitate at low temperature (<40°C) and shallow burial, giving a clear exception to the idea that quartz overgrowth in sandstone reservoirs only precipitates at temperature higher than 80 °C.

Berthierine Crystallization and Reaction Pathway

Berthierine crystallization in sandstone has been interpreted as an early diagenetic process of iron oxy-hydroxide and kaolinite under anoxic conditions (Taylor, 1990; Hornibrook and Longstaffe, 1996). The crystallization of berthierine has been reproduced in experiments by Harder (1989) from iron hydroxide particles in solution under reducing conditions. In addition, pre-burial berthierine-rich clays have been previously reported in Wealden Group sediments on the Isle of Wight, UK (Huggett et al., 2018) and in the Weald basin, UK (Taylor, 1990). In these cases, berthierine crystallization was interpreted as replacing faecal pellets (Huggett et al., 2018) or from iron oxy-hydroxide ooids and kaolinite formed in soils and transported into the basin. In the present study, we believe the berthierine is unambiguously of diagenetic origin. It crystallized (1) as authigenic clay coats around detrital

grains and early eogenetic minerals (Fig. 12); and (2) by replacement of ooid grains (Fig. 9C). To form berthierine, specific chemical elements are required such as Fe and Al in a reducing environment (Hornibrook and Longstaffe, 1996). In our case, berthierine appears to have formed from a source material consisting of aluminous and ferric detrital clays (mainly kaolinite, HIMS) and ferruginous-aluminous ooids (Taylor, 1990; Hornibrook and Longstaffe, 1996; Worden and Morad, 2003; Worden and Burley, 2003; Beaufort et al., 2015; Huggett et al., 2018; Worden et al., 2020).

From the mineralogical characteristics of the Wealden Group sandstones of the Paris Basin, we propose that berthierine is a product of the following reaction:



Furthermore, in the absence of silica released from significant compaction of the sediments, the silica required for the crystallization of the tiny quartz overgrowths formed at the interface between detrital quartz and berthierine clay coats may also be provided by the same mineralogical reaction.

A basic pH ($\text{pH} > 7$) and low pCO_2 compatible with a connate seawater are required for the formation of berthierine (Maynard, 1986). The predominance of Fe^{2+} within berthierine suggests that reducing conditions are necessary (relatively low dissolved oxygen content in pore waters), such as in sub-oxic iron reducing conditions (Worden and Morad, 2003; Worden et al., 2020). We also observe berthierine as ooid grains replacing iron oxy-hydroxide and kaolinite (Fig. 10B-C). Since these sandstones are relatively rich in organic debris and decaying of organic matter that would explain changes of Eh towards reducing conditions. The reduction of iron in ferric and aluminous clays and ooids are prerequisites of prime importance for the crystallization of berthierine. The reduction of ferric iron in octahedral sheets allows the breakdown of the crystal structure of the ferric detrital clays

and the release of Fe^{2+} , Si^{2+} and Mg^{2+} in solution, while maintaining residual aluminous sheets, due to the the very low solubility of Al in diagenetic waters. These residual aluminous sheets form the building blocks for the nucleation and growth of berthierine crystals when the conditions of stability for this mineral are reached.

Within the cores studied, the actual maximum burial depth of Wealden Group sandstones ranges from 450 m (Beynes wells A and B) to 1000 m (CR12). Comparisons between the shallower wells and the deeper well confirmed that berthierine only occurred in well CR12 at 910-922m, not in the shallower wells. The present-day temperature of the CR12 well is 36 °C at a depth of about 900 m. Some studies have shown that the aquifer, located at 900 m depth, has a present-day temperature of about 38–40 °C (Le Nir et al., 2009; Seguin et al., 2015). The burial reconstruction for the CR12 well suggests that the Wealden Group sandstone reservoir is presently at its maximum burial depth, and has probably been at the same depth for 40 m.y. (Fig. 2). Well CR12 has been buried at more than 800 m since 60 Ma, and the studied samples may have only been at a temperature of more than 30–33 °C for 60 m.y. (Fig. 2). Therefore, berthierine and the early quartz overgrowths formed at temperatures ranging from 30 to 36 °C and depths ranging from 850 to 920 m. This zone would mark the transition from unconsolidated sands to lightly consolidated or brittle sandstones.

The Source-To-Sink Control For Berthierine Crystallization

Iron-rich ooids were well-developed in the upper part of the Wealden Group sandstones in the deltaic facies association in all the studied wells. These iron-ooids and ironstones are also reported in the Wealden Group sandstones of the Weald basin, 250 km north-west of the study area (Taylor, 1990; Akinlotan, 2018, 2019), and in the eastern Paris Basin, 150 km east of the study area (Meyer, 1976).

645 Some studies show that thick lateritic weathering soils developed during the Early
646 Cretaceous after successive tectonic events and several sea level falls which resulted in the
647 emersion and erosion of local domains in western Europe (Meyer, 1976; Thiry et al., 2006;
648 Barbarand et al., 2018). Laterite refers to iron oxides and aluminium rich soils whereas
649 ferricrete refers to iron-rich duricrusts in soils, which here are referred to as paleosoils. For
650 example, on the Hercynian basements, thick kaolinitic weathering profiles and ferricrete
651 formed during the Early Cretaceous according to palaeomagnetic dating (Fig. 16, Thiry et al.,
652 2006). Meyer (1976) described the development of soils during the emersion of Wealden
653 Group sediments in the eastern part of the Paris Basin. In addition, very early sideritic
654 ironstones (ferricrete) have been reported from the Wadhurst Clay Formation (Valanginian)
655 within the Weald Basin, SE England (Akinlotan, 2019). These studies suggest that during the
656 Early Cretaceous, periods of emersion in the basin induced continental conditions, which
657 resulted in lateritic weathering, followed by erosion on the basin edges (i.e. Ardennes,
658 Brabant, Central and Armorican Massifs). As several tributaries would have flowed into the
659 Wealden gutter (Thiry et al., 2006), erosion and weathering by-products such as aluminium
660 and iron, may have been deposited into the NW–SE Wealden gutter during deposition of the
661 Wealden Group sandstones (Thiry et al., 2006 and references therein; Fig. 17). Taylor (1990)
662 suggested that iron-ooids or kaolinite ooids resulted from pedogenic processes in laterite
663 soils which were eroded and then transported to the basin. Such pedogenic processes are
664 also very good candidates for the supply of HIMs.

665 The Al may also have originated from the dissolution of Al minerals identified within the
666 Wealden Group sandstone such as kaolinite, smectite, illite or mica (Rivard et al., 2013).
667 Within the samples studied, partly dissolved kaolinite and detrital mica is observed in
668 samples containing diagenetic berthierine (Fig. 12). Concerning Fe availability, detrital HIMs

669 may have also played a role. These minerals are important because their high iron (Fe^{3+})
670 content may have significantly contributed to the source of iron required to form the deeper
671 berthierine (in the Fe^{2+} state). HIMs formation involved in weathering processes are known
672 to have formed thick kaolinitic weathering profiles and ferricrete levels around the Paris
673 Basin during the Early Cretaceous (Meyer, 1976; Thiry et al., 2006). The source-to-sink
674 system in the basin during the Early Cretaceous was conducive to sand sedimentation with a
675 massive supply of iron ooids and kaolinite in the clay assemblage ($\approx 40\%$ of kaolinite on
676 average in the clay assemblage of the Wealden Group sandstones in the Paris Basin). The
677 origin of these Fe-ooids is not easy to characterize and is a continuing problem in
678 sedimentary geology (Sturesson et al., 2000; Di Bella et al., 2019). Iron ooids have been
679 associated with lateritic soil formation in many low latitude areas (Young and Taylor, 1989).
680 Iron ooids in the Wealden Group sandstones of the Paris Basin around Germigny-sur-
681 Coulombs have been documented by Taylor (1996). These ooids were characterized by
682 concentric laminations of goethite around quartz or iron oxide nuclei (Taylor, 1996). Taylor
683 (1996) proposed a marine environment origin for the goethite ooids in the Wealden Group
684 sandstones, suggesting that precipitation occurred on the sea-floor or just below the
685 sediment/marine water interface. A similar process has been suggested by Collin et al.
686 (2005) for the origin of goethite ooids in Jurassic marine environments of the Eastern Paris
687 Basin. In the Wealden Group sandstones, the presence of quartz or ironstone nuclei suggests
688 that the detrital grains (iron fragments and quartz) were most likely derived from the
689 lateritic and ferricrete paleosoils located in the Eastern Paris Basin (Taylor, 1996). Although
690 weathering during a warm climate during the Early Cretaceous is undeniable (Thiry et al.,
691 2006), we believe an eodiagenesis process in estuarine environments, at the sediment
692 surface and accretion of Fe-oxy-hydroxide around nuclei, is a more reasonable explanation

for the origin of goethite ooids (Schiavon, 1988; Taylor, 1996). Iron-oxidizing bacteria and/or fungi could have promoted this eodiagenetic process (Préat et al., 2008). Weathering processes also release kaolinite and HIMs within oxidizing waters, which promotes the particulate transport of Al and Fe into the clastic sedimentary formations (Morad et al., 2000). After shallow burial (here, greater than 800 m), dissolution of the Fe-bearing minerals under reducing condition would release Fe^{2+} in solution to form berthierine by the interaction between dissolved iron in waters and kaolinite during shallow burial (Rivard et al., 2013). Therefore, the contribution of minerals from Al and iron-rich soils (such as HIMs) to the source material appears to play a key role in the formation of berthierine crystallization and thus the subsequent chloritization of the sandstones that will occur at greater burial depths.

Implications for the early Determinism of the Reservoir Qualities of Chloritized Sandstones

Berthierine in the Lower Cretaceous Wealden sediments of the Paris Basin can be considered as a precursor of Fe-rich chlorite coatings (e.g. Worden et al., 2020). With increasing burial depth, berthierine would be converted into Fe-rich chlorite through a chlorite-berthierine mixed as observed in the Springhill sandstones (Early Cretaceous, Argentina, Austral Basin) which were buried to about 2400 m and at a temperature of more than 80 °C (Tinseau, 2002). This berthierine to Fe-Chlorite transformation in sandstones has been reproduced experimentally by Aagaard et al. (2000) and chlorite-berthierine mixed-layers have been reported from XRD investigations in many chloritized sandstone reservoirs around the world (Reynolds, 1988, 1992; Hillier and Velde, 1992; Ryan and Reynolds, 1996; Ryan and Hillier, 2002). Finally, on the basis of high resolution TEM investigations, microstructural models have been proposed to explain the volume-conserving aspect of the

berthierine-to-chlorite reaction and the related formation of chlorite-berthierine mixed layers (Banfield and Bailey, 1996; Xu and Veblen, 1996). Although still debated, it is broadly agreed that the temperature at which Fe-rich chlorite replaces berthierine in natural systems through mixed-layer minerals ranges from 40 to 120 °C (Jahren and Aagaard, 1989; Hillier and Velde, 1992; Ehrenberg, 1993; Aagaard et al., 2000; Worden and Morad, 2003; Beaufort et al., 2015; Šegvić et al., 2020; Worden et al., 2020). Sandstones of the Wealden Group of the Paris Basin whose maximum burial depth and temperature never exceeded 1 km and 40 °C respectively, appear to allow a perfect case study for examining the petrographic and mineralogical characteristics of sandstones which underwent only incipient pre-chloritization processes (i.e. in which replacement of the berthierine precursor by Fe-bearing chlorite has not occurred).

A major finding of this study is that authigenic berthierine coats form at shallow depths and at lower temperatures than that at which the berthierine-to-chlorite conversion is effective and that berthierine grain coats inhibit incipient, low-temperature quartz cementation on detrital quartz grains (Fig. 12C). This means that the key mineral primarily controlling reservoir quality of the deeply buried sandstone reservoirs by inhibiting excessive quartz growth is berthierine, rather than iron-rich chlorite.

CONCLUSIONS

1. Based on detailed petrographic and diagenetic study of the Wealden Group sandstones of the Paris Basin we document formation of berthierine minerals at shallow depths and low temperatures (0.8–1 km and 35–40 °C) prior to the formation of chlorite.

2. The sandstones are mainly feldspathic litharenites deposited in a transgressive sequence of coastal environments ranging from fluvial, estuarine and deltaic environments to shoreface environments.
3. In core samples from 400 m to 600 m depth, sandstones include iron-ooids (goethite), kaolinite and hydroxy-interlayered clay minerals (HIMs). In a different well (CR12) sampled at a depth of 900–970 m, clay minerals are quite different, and include berthierine, which occurs as authigenic clay coats around detrital grains with a typical honeycomb texture. The main controlling factor in the formation of berthierine is burial depth.
4. Small incipient quartz overgrowths were documented on the surface of detrital quartz grains that were buried less than 1 km of burial depth and at temperatures below 40 °C.
5. The arrangement of berthierine crystals at the base of an early clay grain coat appears to have inhibited the development of early quartz overgrowths. Our study reveals that the key mineral controlling reservoir quality of deeply-buried sandstone reservoirs is berthierine, challenging the common assumption that iron-rich chlorite is the most important mineral inhibiting the development of quartz cement. Iron-rich chlorite is known to replace berthierine at depth and high temperatures (>70–80°C) but this study suggests that berthierine is already a decisive factor in inhibiting quartz overgrowth at shallower burial depths.
6. During a period conducive for the development of thick kaolinite-rich weathering profiles or ferricrete, iron-ooids, kaolinite or hydroxy-interlayered clay minerals (HIMs) produced from the lateritic soils were eroded and then transported into the basin. Kaolinite or hydroxy-interlayered clay minerals (HIMs) are key candidates to be

the precursor and source of berthierine. During burial, the crystallization of authigenic berthierine and early quartz overgrowth are associated with the dissolution of kaolinite and Fe-rich HIMs and replacement of iron-ooids under reducing conditions. The reduction of ferric iron (Fe^{3+}) in ferric clays and ooids releases Fe^{2+} which is conducive to the nucleation and growth of berthierine.

7. The source-to-sink context of the Paris Basin during the Early Cretaceous controlled the supply of sands, clays, in particular kaolinite and HIMs, and iron-ooids in the Wealden gutter in the centre of the Paris Basin.

8. Estuarine and deltaic sedimentary environments were ideal for berthierine crystallization, favouring mixing between sands, kaolinite and ferric and aluminium-rich clay assemblages and iron-ooids (and organic matter entrapment, reducing conditions). This study enhances our knowledge both of the mineral reactions involved and mode of formation. This study also shows how understanding mineral reactions in low temperature, shallow burial settings can provide important insights into the key factors that controlling deep reservoir quality.

ACKNOWLEDGEMENTS

This work is the result of collaborative project No P04980 CLAYCOAT 'CLAY COATING in shallow marine clastic deposits to improve reservoir quality prediction' between University Paris-Saclay, Bordeaux INP, University of Bordeaux Montaigne, University of Poitiers and Neptune Energy. This study has benefitted greatly from Neptune Energy funding and from the European Union (ERDF) "Region Nouvelle Aquitaine" (technical support). This work is also supported in part by the "Geothermal water circulation in heterogeneous aquifers" project funded by the "Paris-Saclay Initiative d'Excellence", a state aid program managed by

the Agence Nationale de la Recherche (ANR-11-IDEX- 0003). The authors would also like to thank Philippe Blanc for the high quality thin-sections. We are grateful to Maurice Pagel for fruitful discussions about occurrence of berthierine in sedimentary rocks. We sincerely thank Richard Worden (University of Liverpool), an anonymous reviewer and associate editor Peter Eichhubl (University of Texas at Austin) for their extremely helpful comments and detailed reviews that greatly improved the quality of the original manuscript.

REFERENCES CITED

- Aagaard, P., Jahren, J.S., Harstad, A.O., Nilsen, O., and Ramm, M., 2000, Formation of grain-coating chlorite in sandstones. Laboratory synthesized vs . natural occurrences: *Clay Minerals*, v. 35, p. 261–269, doi:10.1180/000985500546639.
- Aja, S., 2019, Excess functions of chlorite solid solutions and neoformation of Fe-chlorites: Some implications of recent thermochemical measurements: *American Mineralogist*, v. 104, p. 232–243, doi:10.2138/am-2019-6794.
- Akinlotan, O., 2017, Mineralogy and palaeoenvironments: the Weald Basin (Early Cretaceous), Southeast England: *The Depositional Record*, v. 3, p. 187–200, doi:10.1002/dep2.32.
- Akinlotan, O., 2018, Multi-proxy approach to palaeoenvironmental modelling: the English Lower Cretaceous Weald Basin: Palaeoenvironments of the Weald Basin: *Geological Journal*, v. 53, p. 316–335, doi:10.1002/gj.2893.
- Akinlotan, O., 2016, Porosity and permeability of the English (Lower Cretaceous) sandstones: *Proceedings of the Geologists' Association*, v. 127, p. 681–690, doi:10.1016/j.pgeola.2016.10.006.
- Akinlotan, O., 2019, Sideritic ironstones as indicators of depositional environments in the Weald Basin (Early Cretaceous) SE England: *Geological Magazine*, v. 156, p. 533–546, doi:10.1017/S0016756817001017.
- Allen, P., 1959, The Wealden Environment: Anglo-Paris Basin: *Philosophical Transactions of the Royal Society B: Biological Sciences*, v. 242, p. 283–346, doi:10.1098/rstb.1959.0006.
- Allen, P., and Wimbledon, W.A., 1991, Correlation of NW European Purbeck-Wealden (nonmarine Lower Cretaceous) as seen from the English type-areas: *Cretaceous Research*, v. 12, p. 511–526, doi:10.1016/0195-6671(91)90005-W.
- Anjos, S.M.C., De Ros, L.F., and Silva, C.M.A., 2003, Chlorite Authigenesis and Porosity Preservation in the Upper Cretaceous Marine Sandstones of the Santos Basin, Offshore Eastern Brazil, *in* Worden, R.H. and Morad, S. eds., *Clay Mineral Cements in Sandstones*, Oxford, UK, Blackwell Publishing Ltd., p. 289–316, doi:10.1002/9781444304336.ch13.
- Bahlis, A.B., and De Ros, L.F., 2013, Origin and impact of authigenic chlorite in the Upper Cretaceous sandstone reservoirs of the Santos Basin, eastern Brazil: *Petroleum Geoscience*, v. 19, p. 185–199, doi:10.1144/petgeo2011-007.
- Banfield, J.F., and Bailey, S.W., 1996, Formation of regularly interstratified serpentine-

chlorite minerals by tetrahedral inversion in long-period serpentine polytypes: American Mineralogist, v. 81, p. 79–91, doi:10.2138/am-1996-1-211.

Barbarand, J., Bour, I., Pagel, M., Quesnel, F., Delcambre, B., Dupuis, C., and Yans, J., 2018, Post-Paleozoic evolution of the northern Ardenne Massif constrained by apatite fission-track thermochronology and geological data: Bulletin de la Société Géologique de France - Earth Sciences Bulletin, v. 189, p. 16, doi:10.1051/bsgf/2018015.

Barnhisel, R.I., and Bertsch, P.M., 1989, Chlorites and Hydroxy-Interlayered Vermiculite and Smectite, in Dixon, J.B. and Weed, S.B. eds., Minerals in soil environments, Madison, WI, USA, Soil Science Society of America, SSSA Book Series, v. 1, p. 729–788, doi:10.2136/sssabookser1.2ed.c15.

Beaufort, D., Cassagnabere, A., Petit, S., Lanson, B., Berger, G., Lacharpagne, J.C., and Johansen, H., 1998, Kaolinite-to-dickite reaction in sandstone reservoirs: Clay Minerals, v. 33, p. 297–316, doi:10.1180/000985598545499.

Beaufort, D., Rigault, C., Billon, S., Billault, V., Inoue, A., Inoue, S., and Patrier, P., 2015, Chlorite and chloritization processes through mixed-layer mineral series in low-temperature geological systems – a review: Clay Minerals, v. 50, p. 497–523, doi:10.1180/claymin.2015.050.4.06.

Bel, A., Poux, A., Goyénèche, O., Allier, D., Darricau, G., and Lemale, J., 2012, Étude préalable à l’élaboration du schéma de développement de la géothermie en Île-de-France: Bureau de Recherches Géologiques et Minières Rapport final RP-60615-FR, 165 p.

Bergerat, F., Elion, P., Frizon de Lamotte, D., Proudhon, B., Combes, P., André, G., Willeveau, Y., Laurent-Charvet, S., Kourdian, R., Lerouge, G., and Ott d’estevou, P., 2007, 3D multiscale structural analysis of the eastern Paris basin: the Andra contribution, in Lebon, P. ed., A Multi-Disciplinary Approach to the Eastern Jurassic Border of the Paris Basin (Meuse / Haute-Marne), Mémoire de la Société Géologique de France, v. 178, p. 15–35.

Bhattacharyya, D.P., 1983, Origin of Berthierine in Ironstones: Clays and Clay Minerals, v. 31, p. 173–182, doi:10.1346/CCMN.1983.0310302.

Billault, V., Beaufort, D., Baronnet, A., and Lacharpagne, J.-C., 2003, A nanopetrographic and textural study of grain-coating chlorites in sandstone reservoirs: Clay Minerals, v. 38, p. 315–328, doi:10.1180/0009855033830098.

Bloch, S., Lander, R.H., and Bonnell, L., 2002, Anomalous high porosity and permeability in deeply buried sandstone reservoirs: Origin and predictability: AAPG Bulletin, v. 86, p. 301–328.

Bottig, M., Gier, S., and Jilg, W., 2017, Artificially induced clay mineral authigenesis in an underground gas storage field, North Alpine Foreland Basin, Austria: AAPG Bulletin, v. 101, p. 789–806, doi:10.1306/09021615178.

Brigaud, B., Vincent, B., Pagel, M., Gras, A., Noret, A., Landrein, P., and Huret, E., 2018, Sedimentary architecture, depositional facies and diagenetic response to intracratonic deformation and climate change inferred from outcrops for a pivotal period (Jurassic/Cretaceous boundary, Paris Basin, France): Sedimentary Geology, v. 373, p. 48–76, doi:10.1016/j.sedgeo.2018.04.011.

Brindley, G.W., and Brown, G. (Eds.), 1980, Crystal structures of clay minerals and their X-ray identification: London, Mineralogical Society, Mineralogical Society (Great Britain), v. 5, 495 p.

Buissart, H., Clement, B., and Leblanc, M., 1988, Eléments nouveaux sur le faciès wealdien au Nord-Est de Paris: Annales de la Société géologique du Nord, v. 107, p. 155–176.

- Carstea, D.D., 1968, Formation of Hydroxy-Al and -Fe Interlayers in Montmorillonite and Vermiculite: Influence of Particle Size and Temperature: *Clays and Clay Minerals*, v. 16, p. 231–238, doi:10.1346/CCMN.1968.0160305.
- Castro, M.C., Goblet, P., Ledoux, E., Violette, S., and de Marsily, G., 1998, Noble gases as natural tracers of water circulation in the Paris Basin: 2. Calibration of a groundwater flow model using noble gas isotope data: *Water Resources Research*, v. 34, p. 2467–2483, doi:10.1029/98WR01957.
- Collin, P.Y., Loreau, J.P., and Courville, P., 2005, Depositional environments and iron ooid formation in condensed sections (Callovian-Oxfordian, south-eastern Paris basin, France): *Sedimentology*, v. 52, p. 969–985, doi:10.1111/j.1365-3091.2005.00728.x.
- Delineau, T., 1994, FTIR Reflectance vs. EPR Studies of Structural Iron in Kaolinites: *Clays and Clay Minerals*, v. 42, p. 308–320, doi:10.1346/CCMN.1994.0420309.
- Dercourt, J., Gaetani, M., Vrielynck, B., Barrier, E., Biju Duval, B., Brunet, M.F., Cadet, J.P., Crasquin, S., and Sandulescu, M., 2000, Atlas Peri-Tethys, Palaeogeographical maps, 24 maps and explanatory notes: I-XX: CCGM/CGMW, Paris, p. 1–269.
- Di Bella, M., Sabatino, G., Quartieri, S., Ferretti, A., Cavalazzi, B., Barbieri, R., Foucher, F., Messori, F., and Italiano, F., 2019, Modern Iron Ooids of Hydrothermal Origin as a Proxy for Ancient Deposits: *Scientific Reports*, v. 9, p. 7107, doi:10.1038/s41598-019-43181-y.
- Dixon, S.A., Summers, D.M., and Surdam, R.C., 1989, Diagenesis and Preservation of Porosity in Nepheloid Formation (Upper Jurassic), Southern Alabama: *AAPG Bulletin*, v. 73, doi:10.1306/44B4A24E-170A-11D7-8645000102C1865D.
- Dowey, P.J., Hodgson, D.M., and Worden, R.H., 2012, Pre-requisites, processes, and prediction of chlorite grain coatings in petroleum reservoirs: A review of subsurface examples: *Marine and Petroleum Geology*, v. 32, p. 63–75, doi:10.1016/j.marpetgeo.2011.11.007.
- Duteil, T., Bourillot, R., Grégoire, B., Virolle, M., Brigaud, B., Nouet, J., Braissant, O., Portier, E., Fénies, H., Patrier, P., Gontier, E., Svahn, I., and Visscher, P.T., 2020, Experimental formation of clay-coated sand grains using diatom biofilm exopolymers: *Geology*, v. 48, p. 1012–1017, doi:10.1130/G47418.1.
- Ehrenberg, S.N., 1993, Preservation of anomalously high porosity in deeply buried sandstones by grain-coating chlorite: examples from the Norwegian continental shelf: *AAPG Bulletin*, v. 77, p. 1260–1286.
- Folk, R.L., 1974, *Petrology of sedimentary rocks*: Austin, Texas, Hemphill Publishing Company, v. 182, 184 p.
- Gély, J.-P., and Hanot, F., 2014, Coupe géologique du Bassin parisien et du Fossé rhénan, in *Le Bassin parisien, un nouveau regard sur la géologie*, Paris, Association des Géologues du Bassin de Paris, Bull. Inf. Géol. Bass. Paris, Mémoire hors-série, v. 9, p. 1 plate.
- Gould, K., Pe-Piper, G., and Piper, D.J.W., 2010, Relationship of diagenetic chlorite rims to depositional facies in Lower Cretaceous reservoir sandstones of the Scotian Basin: *Sedimentology*, v. 57, p. 587–610, doi:10.1111/j.1365-3091.2009.01106.x.
- Griffiths, J., Worden, R.H., Wooldridge, L.J., Utley, J.E.P., and Duller, R.A., 2019, Compositional variation in modern estuarine sands: Predicting major controls on sandstone reservoir quality: *AAPG Bulletin*, v. 103, p. 797–833, doi:10.1306/09181818025.
- Griffiths, J., Worden, R.H., Wooldridge, L.J., Utley, J.E.P., and Duller, R.A., 2018a, Detrital Clay Coats, Clay Minerals, and Pyrite: A Modern Shallow-Core Analogue For Ancient and

- Deeply Buried Estuarine Sandstones: *Journal of Sedimentary Research*, v. 88, p. 1205–1237, doi:10.2110/jsr.2018.56.
- Griffiths, J., Worden, R.H., Wooldridge, L.J., Utley, J.E.P., Duller, R.A., and Edge, R.L., 2018b, Estuarine clay mineral distribution: Modern analogue for ancient sandstone reservoir quality prediction: *Sedimentology*, doi:10.1111/sed.12571.
- Guillocheau, F., Robin, C., Allemand, P., Bourquin, S., Brault, N., Dromart, G., Friedenber, R., Garcia, J.-P., Gaulier, J.-M., Gaumet, F., Grosdoy, B., Hanot, F., Le Strat, P., Mettraux, M., Nalpas, T., Prijac, C., Rigoltet, C., Serrano, O., and Grandjean, G., 2000, Meso-Cenozoic geodynamic evolution of the Paris Basin: 3D stratigraphic constraints: *Geodinamica Acta*, v. 13, p. 189–245, doi:10.1080/09853111.2000.11105372.
- Haile, B.G., Hellevang, H., Aagaard, P., and Jahren, J., 2015, Experimental nucleation and growth of smectite and chlorite coatings on clean feldspar and quartz grain surfaces: *Marine and Petroleum Geology*, v. 68, p. 664–674, doi:10.1016/j.marpetgeo.2015.02.006.
- Harder, H., 1989, Mineral genesis in ironstones: a model based upon laboratory experiments and petrographic observations: Geological Society, London, Special Publications, v. 46, p. 9–18, doi:10.1144/GSL.SP.1989.046.01.04.
- Hillier, S., and Velde, B., 1992, Chlorite interstratified with a 7 Å mineral: an example from offshore Norway and possible implications for the interpretation of the composition of diagenetic chlorites: *Clay Minerals*, v. 27, p. 475–486, doi:10.1180/claymin.1992.027.4.07.
- Hornibrook, E.R.C., and Longstaffe, F.J., 1996, Berthierine from the Lower Cretaceous Clearwater Formation, Alberta, Canada: *Clays and Clay Minerals*, v. 44, p. 1–21, doi:10.1346/CCMN.1996.0440101.
- Huggett, J.M., Gale, A.S., and Hazell, C., 2018, Early diagenesis of the lower Vectis Formation, Wealden Group Lower Cretaceous, Barremian), Sandown, Isle of Wight: *Proceedings of the Geologists' Association*, v. 129, p. 782–789, doi:https://doi.org/10.1016/j.pgeola.2018.08.004.
- Jacquín, T., Rusciadelli, G., Amedro, F., de Graciansky, P.-C., and Magniez-Jannin, F., 1998, The North Atlantic cycle: an overview of 2nd-order transgressive/regressive facies cycles in the Lower Cretaceous of Western Europe, *in* de Graciansky, P.-C., Hardenbol, J., Jacquín, T., and Vail, P.R. eds., *Mesozoic and Cenozoic Sequence Stratigraphy of European Basins*, SEPM Special Publication, v. 60, p. 397–409.
- Jahren, J.S., and Aagaard, P., 1989, Compositional Variations in Diagenetic Chlorites and Illites, and Relationships with Formation-Water Chemistry: *Clay Minerals*, v. 24, p. 157–170, doi:10.1180/claymin.1989.024.2.04.
- Lander, R.H., Larese, R.E., and Bonnell, L.M., 2008, Toward more accurate quartz cement models: The importance of euhedral versus noneuhedral growth rates: *AAPG Bulletin*, v. 92, p. 1537–1563, doi:10.1306/07160808037.
- Lander, R.H., and Walderhaug, O., 1999, Predicting Porosity through Simulating Sandstone Compaction and Quartz Cementation: *AAPG Bulletin*, v. 83, p. 433–449, doi:10.1306/00AA9BC4-1730-11D7-8645000102C1865D.
- Lanson, B., Ferrage, E., Hubert, F., Prêt, D., Mareschal, L., Turpault, M.-P., and Ranger, J., 2015, Experimental aluminization of vermiculite interlayers: An X-ray diffraction perspective on crystal chemistry and structural mechanisms: *Geoderma*, v. 249–250, p. 28–39, doi:10.1016/j.geoderma.2015.03.005.
- Larese, R.E., Pittman, E.D., and Heald, M.T., 1984, Effects of Diagenesis on Porosity

967 Development, Tuscaloosa Sandstone, Louisiana: AAPG Bulletin, v. 68,
 968 doi:10.1306/AD460F12-16F7-11D7-8645000102C1865D.
 969 Le Nir, M., S. Bézégues, Ranquet, C., Szymanski, A.L., Darricau, G., and Lemale, J., 2009,
 970 Ressources géothermiques du département de l'Essonne (91): Bureau de Recherches
 971 Géologiques et Minières RP-56966-FR, 295 p.
 972 Mackenzie, K.J.D., and Berezowski, R.M., 1984, Thermal and Mössbauer studies of iron-
 973 containing hydrous silicates. V. Berthierine: *Thermochimica Acta*, v. 74, p. 291–312,
 974 doi:10.1016/0040-6031(84)80030-1.
 975 Maynard, J.B., 1986, Geochemistry of oolitic iron ores, an electron microprobe study:
 976 *Economic Geology*, v. 81, p. 1473–1483, doi:10.2113/gsecongeo.81.6.1473.
 977 McKay, J.L., and Longstaffe, F.J., 2003, Sulphur isotope geochemistry of pyrite from the
 978 Upper Cretaceous Marshybank Formation, Western Interior Basin: *Sedimentary*
 979 *Geology*, v. 157, p. 175–195, doi:10.1016/S0037-0738(02)00233-6.
 980 Mégnien, C., and Mégnien, F., 1980, Synthèse géologique du Bassin de Paris: Orléans,
 981 Mémoire du BRGM, v. 101, 446 p.
 982 Meunier, A., Sardini, P., Robinet, J.C., and Prêt, D., 2007, The petrography of weathering
 983 processes: facts and outlooks: *Clay Minerals*, v. 42, p. 415–435,
 984 doi:10.1180/claymin.2007.042.4.01.
 985 Meyer, R., 1976, Continental sedimentation, soil genesis and marine transgression in the
 986 basal beds of the Cretaceous in the east of the Paris Basin: *Sedimentology*, v. 23, p.
 987 235–253, doi:10.1111/j.1365-3091.1976.tb00048.x.
 988 Morad, S., Al-Ramadan, K., Ketzer, J.M., and De Ros, L.F., 2010, The impact of diagenesis on
 989 the heterogeneity of sandstone reservoirs: A review of the role of depositional facies
 990 and sequence stratigraphy: *AAPG Bulletin*, v. 94, p. 1267–1309.
 991 Morad, S., Ketzer, J.M., and De Ros, L.F., 2000, Spatial and temporal distribution of
 992 diagenetic alterations in siliciclastic rocks: implications for mass transfer in
 993 sedimentary basins: *Diagenetic alterations in siliciclastic rocks: Sedimentology*, v. 47, p.
 994 95–120, doi:10.1046/j.1365-3091.2000.00007.x.
 995 Odin, G.S., 1988, Green Marine Clays: Oolitic Ironstone Facies, Verdine Facies, Glaucony
 996 Facies and Celadonite-Bearing Rock Facies-A Comparative Study: Elsevier, 445 p.
 997 Odin, G.S., and Matter, A., 1981, De glauconiarum origine: *Sedimentology*, v. 28, p. 611–641,
 998 doi:10.1111/j.1365-3091.1981.tb01925.x.
 999 Pittman, E.D., and Lumsden, D.N., 1968, Relationship between chlorite coatings on quartz
 1000 grains and porosity, Spiro Sand, Oklahoma: *Journal of Sedimentary Research*, v. 38, p.
 1001 668–670, doi:10.1306/74D71A28-2B21-11D7-8648000102C1865D.
 1002 Porrenga, D.H., 1967, Glauconite and chamosite as depth indicators in the marine
 1003 environment: *Marine Geology*, v. 5, p. 495–501, doi:10.1016/0025-3227(67)90056-4.
 1004 Prétat, A., El Hassani, A., and Mamet, B., 2008, Iron bacteria in Devonian carbonates (Tafilalt,
 1005 Anti-Atlas, Morocco): *Facies*, v. 54, p. 107–120, doi:10.1007/s10347-007-0124-2.
 1006 Reynolds, R., 1988, Mixed layer chlorite minerals. In *Hydrous phyllosilicates: Reviews in*
 1007 *Mineralogy*, v. 19, p. 601–629.
 1008 Reynolds, R.C., 1992, Randomly Interstratified Serpentine/Chlorite: Its Detection and
 1009 Quantification by Powder X-ray Diffraction Methods: *Clays and Clay Minerals*, v. 40, p.
 1010 262–267, doi:10.1346/CCMN.1992.0400302.
 1011 Rivard, C., Pelletier, M., Michau, N., Razafitianamaharavo, A., Bihannic, I., Abdelmoula, M.,
 1012 Ghanbaja, J., and Villieras, F., 2013, Berthierine-like mineral formation and stability
 1013 during the interaction of kaolinite with metallic iron at 90°C under anoxic and oxic

- conditions: *American Mineralogist*, v. 98, p. 163–180, doi:10.2138/am.2013.4073.
- Roduit, N., 2007, JMicroVision: un logiciel d'analyse d'images pétrographiques polyvalent: Section de Sciences de la Terre, Université de Genève, 116 p., 10.13097/archive-ouverte/unige:468.
- Rusciadelli, G., 1996, Stratigraphie séquentielle et modélisation de l'espace disponible du Jurassique supérieur et du Crétacé inférieur du Bassin de Paris: Université Paris-Sud, 200 p.
- Ryan, P.C., and Hillier, S., 2002, Berthierine/chamosite, corrensite, and discrete chlorite from evolved verdine and evaporite-associated facies in the Jurassic Sundance Formation, Wyoming: *American Mineralogist*, v. 87, p. 1607–1615, doi:10.2138/am-2002-11-1210.
- Ryan, P.C., and Reynolds, J., 1996, The origin and diagenesis of grain-coating serpentine-chlorite in Tuscaloosa Formation sandstone, US Gulf Coast: *American Mineralogist*, v. 81, p. 213–225.
- Saïag, J., Brigaud, B., Portier, É., Desaubliaux, G., Bucherie, A., Miska, S., and Pagel, M., 2016, Sedimentological control on the diagenesis and reservoir quality of tidal sandstones of the Upper Cape Hay Formation (Permian, Bonaparte Basin, Australia): *Marine and Petroleum Geology*, v. 77, p. 597–624, doi:10.1016/j.marpetgeo.2016.07.002.
- Schiavon, N., 1988, Goethite ooids: growth mechanism and sandwave transport in the Lower Greensand (early Cretaceous, southern England): *Geological Magazine*, v. 125, p. 57–62, doi:10.1017/S0016756800009377.
- Seguin, J.J., Castillo, C., and Arnaud, L., 2015, Modélisation des nappes de l'Albien et du Néocomien: Bureau de Recherches Géologiques et Minières Rapport final RP-64873-F, 271 p.
- Šegvić, B., Zanon, G., and Moscariello, A., 2020, On the origins of eogenetic chlorite in verdine facies sedimentary rocks from the Gabon Basin in West Africa: *Marine and Petroleum Geology*, v. 112, p. 104064, doi:10.1016/j.marpetgeo.2019.104064.
- Sturesson, U., Heikoop, J.M., and Risk, M.J., 2000, Modern and Palaeozoic iron ooids—a similar volcanic origin: *Sedimentary Geology*, v. 136, p. 137–146, doi:10.1016/S0037-0738(00)00091-9.
- Taylor, K.G., 1990, Berthierine from the non-marine Wealden (Early Cretaceous) sediments of south-east England: *Clay Minerals*, v. 25, p. 391–399, doi:10.1180/claymin.1990.025.3.13.
- Taylor, K.G., 1996, Early Cretaceous iron ooids in the Paris Basin: pedogenic versus marine origin and their palaeoclimatic significance: *Cretaceous Research*, v. 17, p. 109–118, doi:10.1006/cres.1996.0009.
- Thiry, M., Quesnel, F., Yans, J., Wyns, R., Vergari, A., Theveniaut, H., Simon-Coinçon, R., Ricordel, C., Moreau, M.-G., Giot, D., Dupuis, C., Bruxelles, L., Barbarand, J., and Baele, J.-M., 2006, Continental France and Belgium during the early Cretaceous: paleoweatherings and paleolandforms: *Bulletin de la Société Géologique de France*, v. 177, p. 155–175, doi:10.2113/gssgfbull.177.3.155.
- Tinseau, E., 2002, Processus sédimentaires et diagénétiques à l'origine de la formation des chlorites dans les réservoirs silicoclastiques: Université Paris-Sud, 287 p., <https://www.theses.fr/2002PA112246>.
- Torelli, M., Traby, R., Teles, V., and Ducros, M., 2020, Thermal evolution of the intracratonic Paris Basin: Insights from 3D basin modelling: *Marine and Petroleum Geology*, v. 119, p. 104487, doi:10.1016/j.marpetgeo.2020.104487.
- Van Houten, F.B., and Purucker, M.E., 1984, Glauconitic peloids and chamositic ooids -

1061 favorable factors, constraints, and problems: *Earth-Science Reviews*, v. 20, p. 211–243,
 1062 doi:10.1016/0012-8252(84)90002-3.

1063 Velde, B., 1985, *Clay minerals: a physico-chemical explanation of their occurrence:*
 1064 Amsterdam, Elsevier, *Developments in Sedimentology*, v. 40, 427 p.

1065 Vernoux, J.F., Maget, P., Afzali, H., Blanchin, R., Donsimoni, M., and Vairon, J., 1997,
 1066 *Synthèse hydrogéologique du Crétacé inférieur du bassin de Paris: Bureau de*
 1067 *Recherches Géologiques et Minières rapport BRGM DSGR/IDF R39702*, 93 p.

1068 Viennet, J.-C., Hubert, F., Ferrage, E., Tertre, E., Legout, A., and Turpault, M.-P., 2015,
 1069 Investigation of clay mineralogy in a temperate acidic soil of a forest using X-ray
 1070 diffraction profile modeling: Beyond the HIS and HIV description: *Geoderma*, v. 241–
 1071 242, p. 75–86, doi:10.1016/j.geoderma.2014.11.004.

1072 Viennet, J.-C., Hubert, F., Tertre, E., Ferrage, E., Robin, V., Dzene, L., Cochet, C., and Turpault,
 1073 M.-P., 2016, Effect of particle size on the experimental dissolution and auto-
 1074 aluminization processes of K-vermiculite: *Geochimica et Cosmochimica Acta*, v. 180, p.
 1075 164–176, doi:10.1016/j.gca.2016.02.005.

1076 Virolle, M., Brigaud, B., Bourillot, R., Féliès, H., Portier, E., Duteil, T., Nouet, J., Patrier, P.,
 1077 and Beaufort, D., 2019a, Detrital clay grain coats in estuarine clastic deposits: origin
 1078 and spatial distribution within a modern sedimentary system, the Gironde Estuary
 1079 (south-west France): *Sedimentology*, v. 66, p. 859–894, doi:10.1111/sed.12520.

1080 Virolle, M., Brigaud, B., Luby, S., Portier, E., Féliès, H., Bourillot, R., Patrier, P., and Beaufort,
 1081 D., 2019b, Influence of sedimentation and detrital clay grain coats on chloritized
 1082 sandstone reservoir qualities: Insights from comparisons between ancient tidal
 1083 heterolithic sandstones and a modern estuarine system: *Marine and Petroleum*
 1084 *Geology*, v. 107, p. 163–184, doi:10.1016/j.marpetgeo.2019.05.010.

1085 Virolle, M., Féliès, H., Brigaud, B., Bourillot, R., Portier, E., Patrier, P., Beaufort, D., Jalon-
 1086 Rojas, I., Derriennic, H., and Miska, S., 2020, Facies associations, detrital clay grain
 1087 coats and mineralogical characterization of the Gironde estuary tidal bars: A modern
 1088 analogue for deeply buried estuarine sandstone reservoirs: *Marine and Petroleum*
 1089 *Geology*, p. 104225, doi:https://doi.org/10.1016/j.marpetgeo.2020.104225.

1090 Walderhaug, O., 1996, Kinetic Modeling of Quartz Cementation and Porosity Loss in Deeply
 1091 Buried Sandstone Reservoirs: *AAPG Bulletin*, v. 80, p. 731–745,
 1092 doi:10.1306/64ED88A4-1724-11D7-8645000102C1865D.

1093 Walderhaug, O., 1994a, Precipitation rates for quartz cement in sandstones determined by
 1094 fluid-inclusion microthermometry and temperature-history modeling: *Journal of*
 1095 *Sedimentary Research*, v. 64, p. 324–333, doi:10.2110/jsr.64.324.

1096 Walderhaug, O., 1994b, Temperatures of Quartz Cementation in Jurassic Sandstones from
 1097 the Norwegian Continental Shelf-Evidence from Fluid Inclusions: *Journal of*
 1098 *Sedimentary Research*, v. 64, p. 311–323, doi:10.1306/D4267D89-2B26-11D7-
 1099 8648000102C1865D.

1100 Walderhaug, O., Lander, R.H., Bjrkum, P.A., Oelkers, E.H., Bjrykke, K., and Nadeau, P.H.,
 1101 2000, Modelling Quartz Cementation and Porosity in Reservoir Sandstones: Examples
 1102 from the Norwegian Continental Shelf, *in* Worden, R.H. and Morad, S. eds., *Quartz*
 1103 *Cementation in Sandstones*, Oxford, UK, Blackwell Publishing Ltd., p. 39–49,
 1104 doi:10.1002/9781444304237.ch3.

1105 Wooldridge, L.J., Worden, R.H., Griffiths, J., and Utley, J.E.P., 2017, Clay-Coated Sand Grains
 1106 In Petroleum Reservoirs: Understanding Their Distribution Via A Modern Analogue:
 1107 *Journal of Sedimentary Research*, v. 87, p. 338–352, doi:10.2110/jsr.2017.20.

- Wooldridge, L.J., Worden, R.H., Griffiths, J., Utley, J.E.P., and Thompson, A., 2018, The origin of clay-coated sand grains and sediment heterogeneity in tidal flats: *Sedimentary Geology*, v. 373, p. 191–209, doi:10.1016/j.sedgeo.2018.06.004.
- Worden, R.H., and Burley, S.D., 2003, Sandstone Diagenesis: The Evolution of Sand to Stone, *in* Burley, S.D. and Worden, R.H. eds., *Sandstone Diagenesis*, Oxford, UK, Blackwell Publishing Ltd., p. 1–44, doi:10.1002/9781444304459.ch.
- Worden, R.H., Griffiths, J., Wooldridge, L.J., Utley, J.E.P., Lawan, A.Y., Muhammed, D.D., Simon, N., and Armitage, P.J., 2020, Chlorite in sandstones: *Earth-Science Reviews*, v. 204, p. 103105, doi:10.1016/j.earscirev.2020.103105.
- Worden, R.H., and Morad, S., 2003, Clay Minerals in Sandstones: Controls on Formation, Distribution and Evolution, *in* Worden, R.H. and Morad, S. eds., *Clay Mineral Cements in Sandstones*, Oxford, UK, Blackwell Publishing Ltd., p. 3–41, doi:10.1002/9781444304336.ch1.
- Xu, H., and Veblen, D.R., 1996, Interstratification and other reaction microstructures in the chlorite-berthierine series: *Contributions to Mineralogy and Petrology*, v. 124, p. 291–301, doi:10.1007/s004100050192.
- Young, T.P., and Taylor, E.G., 1989, Phanerozoic ironstones: an introduction and review, *in* *Phanerozoic Ironstones*, Geological Society Special Publication 46, v. 127, p. 251, <https://doi.org/10.1017/S0016756800014072>.

FIGURE CAPTIONS

Figure 1: A- Geological map and generalized column for the Paris Basin (scale 1:1,000,000), showing the location (black stars) of the five Wealden Group sandstone wells examined in this study. FO= Fouilleuse wells (FO-01 and FO-06), Beynes wells (A & B), and CR= Crouy-sur-Ourcq well (CR12). B- West-East geological cross section of the Paris Basin, modified after Gély and Hanot (2014). Well CR12 is projected onto the cross-section. C- Palaeogeographical map of the Paris basin during the Hauterivian stage, (modified from Dercourt et al., 2000).

Figure 2: Burial history curve for the CR12 well at Crouy-sur-Ourcq, Paris Basin (decompaction not computed). The geothermal gradient at 2.6 °C/100 m is based on the present-day temperature of 35.5 °C in the well at a depth of 900 m.

Figure 3: Composite log from well CR12 (Crouy-sur-Ourcq) showing location of samples, average grain size, sedimentary structures, faunal assemblages, corresponding palaeo-

environment interpretation; well log gamma-ray; interpreted transgressive/regressive cycles (derived from Rusciadelli, 1996); dominant clay types (XRD<2 µm fraction); and estimated grain coat coverage for selected samples.

Figure 4 : Core photographs showing primary facies in : A- Facies association FA1 (Fluvial) (Well CR12 #CR-03 – 967.70 m) Medium grained, through-cross bedded sandstones, with granules and organic debris. B- FA1 (Fluvial) (Well CR12 #CR-02 – 971.90 m) Muddy siltstones, with coal debris and deformed and compacted root trace. C Facies association FA2 (Estuarine) (Well CR12 #CR-19 – 904.45 m) Medium-grained sandstones with foresets underlined by organic debris (black arrows) interpreted as small tidal dunes. Trace fossils include *Teichichnus* (Te), *Psilonichnus* (Psi) and *Palaeophycus* (Pa). The top of dunes appears eroded and largely bioturbated. D- FA2 (Estuarine) (Well FO-01 – 454.30 m) Fine to medium grained; current-rippled sandstones with tidal mud couplets (arrows). E- FA2 (Estuarine) (Well A – 417.80 m) Fine grained sandstones with visible current ripples (CR) and silty-clay drapes (arrows). F- FA2 (Estuarine) (Well CR12 – 940.60 m) Heterolithic fine grained, wavy bedded (WB) sandstones with clay drapes. Low biodiversity bioturbations (*Planolites*: Pl). G- FA2 (Estuarine) (Well CR12– 914.5 m) Very fine to fine grained sandstones, with clay drapes, lenticular bedding (LB), wavy bedding (WB) and flaser bedding (FB). H- Facies association FA3 (Deltaic) (Well CR12- 978.50 m) Alternating claystone and silty to very fine-grained, current-rippled sandstone, with syneresis cracks (SC) and *Planolites* (Pl). I- Facies association FA4 (Shoreface) (Well CR12 – 897-899 m) Well sorted, medium to coarse-grained sandstones with low angle cross stratification and visible *Skolithos* burrows (arrow).

Figure 5: Quartz, Feldspar, Lithic (QFL) ternary diagrams with samples from the five studied wells after the Classification of Folk (1974). Key to Facies Nomenclature: FA1-Fluvial, FA2-Estuarine; FA-3-Deltaic; FA5-Offshore

Figure 6: Thin section and Scanning Electron Microscopy (SEM) photomicrographs from fluvial and estuarine samples. A- Thin section image showing clay-coated sand grains (quartz, feldspars and lithics) with visible bridges or aggregates (Well CR12, sample CR12-04, 956 m). B- SEM photomicrograph showing clay-coated quartz grain, with visible ridges and/or aggregated clay coats (Well CR12, sample CR12-04, 957 m). C- SEM photomicrograph showing aggregated clay coat on detrital quartz grain (Well CR12, sample CR12-12, 931 m). D- Closeup view of C showing that coatings are mainly composed of clay minerals. E- Thin Section image of greensand containing abundant compacted green peloids (Well FO-06, sample FO-06-17, 487.7 m). F- Backscatter SEM image of polished thin section showing clay grain coats and bridges (Well FO-06, sample FO-06-12, 498.2 m). G- Thin section image of iron-oid facies showing ooids of goethite (G), (Well FO-01, sample FO-01-10, 448 m). H- SEM photomicrograph showing detrital quartz (Qz) grain coated by successive laminae of goethite (well FO-06, sample FO-06-15, 490 m). Key: Qz.= Quartz; Fd= Feldspars; G = Goethite; Gp = Green peloids.

Figure 7: Chart showing average clay coat coverage by facies. The total coat coverage classes are shown above the histograms for each facies. Visual coat coverage estimates are summarized in Legend.

Figure 8: X-Ray diffractograms of the pre-burial clays extracted from Wealden Group sandstones. A.D. = Air Dried; E.G. = Ethylene-Glycol.

Figure 9: Ternary diagrams of the point chemical analyses for the different types of clay particles identified in pre-burial and diagenetic clay coats of the Wealden Group sandstones. A- MR^{3+} - $2R^{3+}$ - $3R^{2+}$ diagram (Velde 1985). B- Al-Fe-Mg diagram. Iron has been arbitrarily considered as Fe^{3+} in pre-burial clay particles and Fe^{2+} in diagenetic clay particles.

Figure 10: Thin section and SEM photomicrographs from estuarine samples showing: A- SEM view of framboidal pyrite (Py) embedded within clay coat with ridged texture (Well CR12, sample CR12-12, 931.1 m). B- Backscatter SEM view of pyrite (Py) embedded within clay coating, a partially dissolved iron-rich ooid, and pore-bridging clay (white arrow), (Well CR12, sample CR12-11, 934 m). C- Thin section image showing small diagenetic siderite rhombs (white arrow) intermixed with clay grain coat on a detrital quartz grain (Well CR12, sample CR12-18, 909 m). D-F- SEM views showing morphology of rhombic siderite on quartz (Well CR12, sample CR12-18, 909 m). G- Thin section image showing patchy ankerite grain coat (Well FO1, sample FO1-09, 453.9 m). H-I -SEM views showing the morphology of patchy ankerite on detrital grain (Well FO1, sample FO1-09, 453.9 m). J- SEM view showing framboidal pyrite intermixed with clay coat. Framboidal or cubic pyrite was observed associated with both types of Fe-carbonates. Well FO1, sample FO1-09, 453.9 m). Key: Qz.= Quartz Py. = Pyrite; Fd = Feldspar

Figure 11: A-B- SEM images showing vermicular kaolinite (arrow) intermixed with detrital clay coats partially filling a pore in fluvial facies (FA1), (Well FO-01, sample FO-01-03, 505 m).

1212 C- Composite FTIR spectra of samples from well FO-01 in the OH-stretching bands region
1213 showing decreasing structural ferric iron content and increasing crystallinity of kaolinite with
1214 increasing depth.

1215

1216 **Figure 12:** SEM images of authigenic clay coats in sample CR12-14 from the estuarine facies.
1217 A- Low magnification view of clay-coated grains. B- Closeup showing honeycomb
1218 morphology of iron-rich berthierine coating intermixed with framboidal pyrite and
1219 vermicular kaolinite. C- SEM image of an ultra-thin FIB section showing the contact between
1220 iron-rich clay minerals (berthierine) and the detrital quartz grain small incipient quartz
1221 overgrowths that appear to be inhibited by the crystallization of the early berthierine clay
1222 coat.

1223

1224 **Figure 13:** Comparison of air-dried (A.D.) and ethylene glycol (E.G.) saturated, oriented XRD
1225 pattern of berthierine-bearing clay material ($<2\ \mu\text{m}$) from an estuarine sandstones buried at
1226 a depth exceeding 900m (Well CR12, sample CR12-18, 909.8m). Key: HIMs = hydroxy-
1227 interlayered clay minerals; solid bar = theoretical 00ℓ reflection of berthierine; dotted bars =
1228 theoretical 00ℓ reflections of berthierine.

1229 **Figure 14:** Comparison showing XRD patterns of randomly oriented clays from sandstones
1230 buried in shallow wells (Well B, sample B-06 at 423.7 m and Well FO-06, sample FO-06-12 at
1231 426.2 m) compared to deeper well CR12 (Well CR12, samples CR12-18 at 909.8 m and CR12-
1232 14 at 922.3 m). A- Diffractograms show difference between kaolinite reflections (dotted
1233 lines) and berthierine reflections (solid lines). The solid lines marked with an asterisk
1234 correspond to the XRD reflections of berthierine which do not overlap with reflections of
1235 kaolinite or any other types of 2:1 dioctahedral phyllosilicates (such as HIMs or illite). B-

1236 Closeup of the XRD peaks in the angular region of 060 reflection for phyllosilicates (58-64°
1237 2θ, Cu Kα). Miller indices are indicated for each hk reflection.

1238

1239 **Figure 15:** FTIR spectra comparing the clay fraction for different estuarine samples in Well
1240 CR12. Berthierine has been identified by SEM observations and X-ray diffraction in each of
1241 these samples (CR12-14, CR12-18 and CR12-19).

1242

1243 **Figure 16:** Paragenetic sequence for the Wealden Group sandstones in the Paris Basin. A list of
1244 potential pre-burial aluminium/iron-rich minerals includes: Fe-Al ooids; Fe-bearing kaolinite;
1245 and Hydroxy-interlayered clay minerals (HIMs).

1246

1247 **Figure 17:** A- Palaeogeographic map of France and Belgium during the Early Cretaceous
1248 period showing palaeo-weathering zones (from Thiry et al., 2006). B- NW–SE transect (A-A'
1249 on map A) showing structure of the Wealden gutter and its edges during the Barremian
1250 (from Thiry et al., 2006).

1251

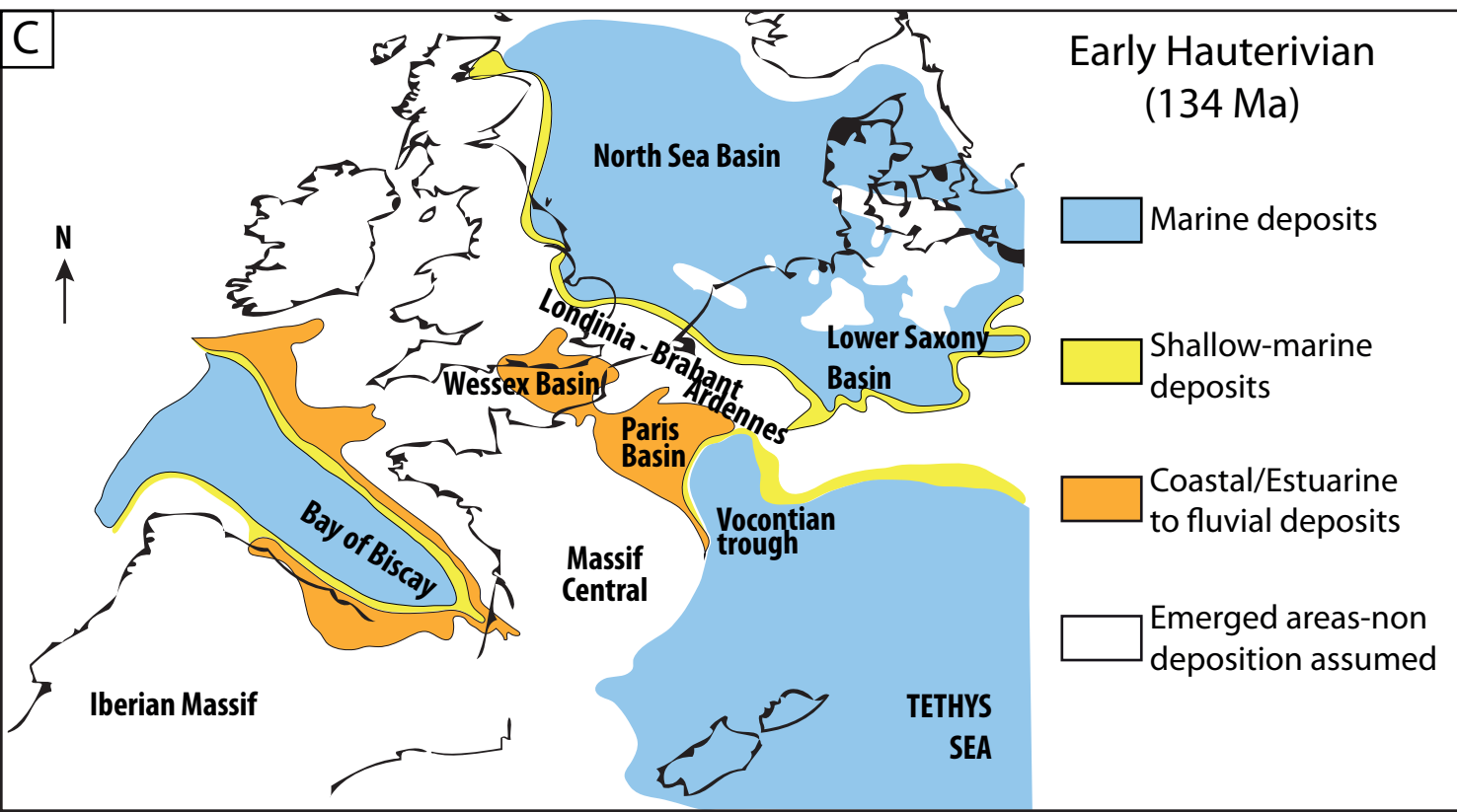
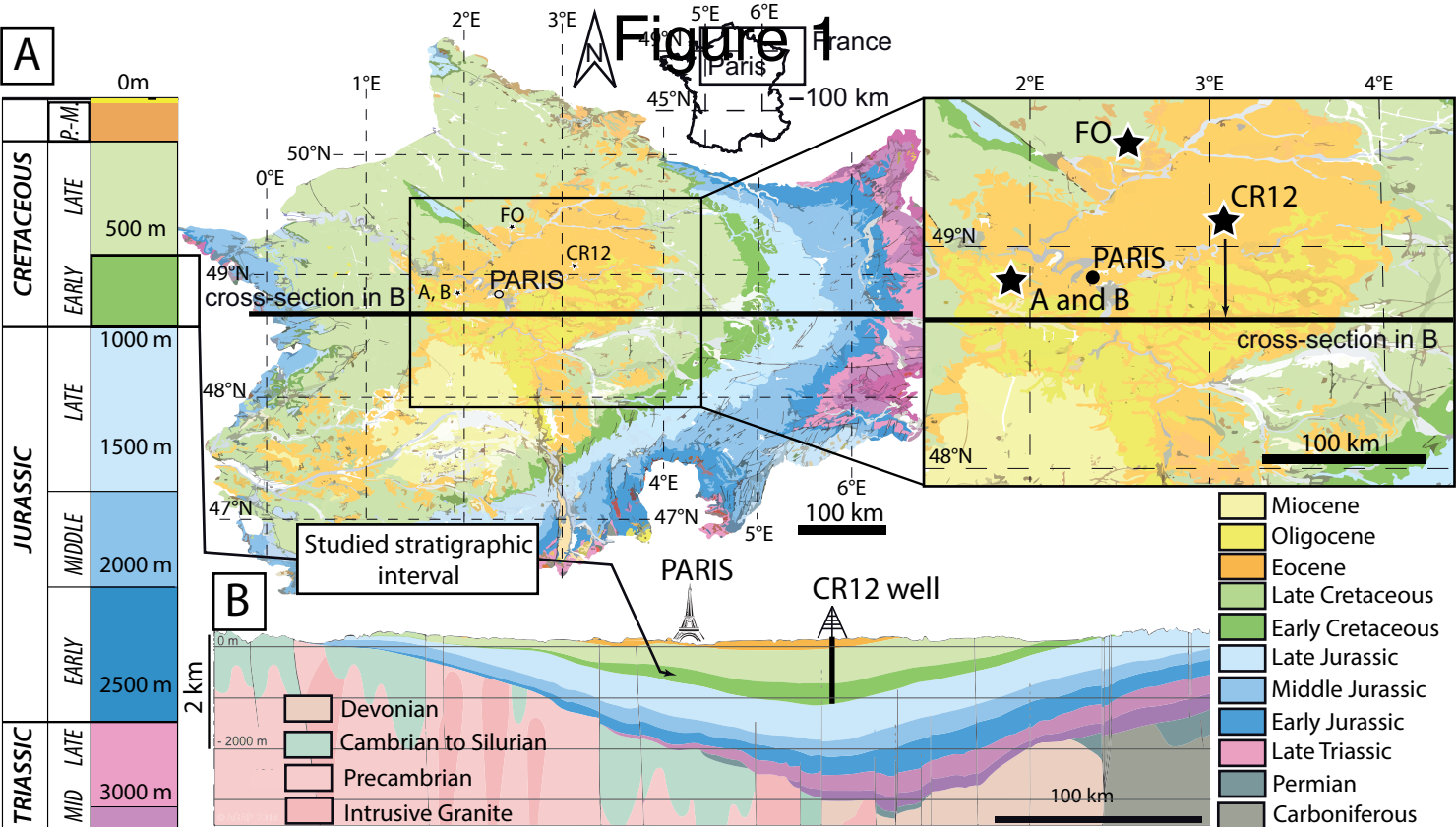
1252 **Table 1:** Summary of facies and facies association identified in the Wealden Group
1253 sandstones of the Paris Basin.

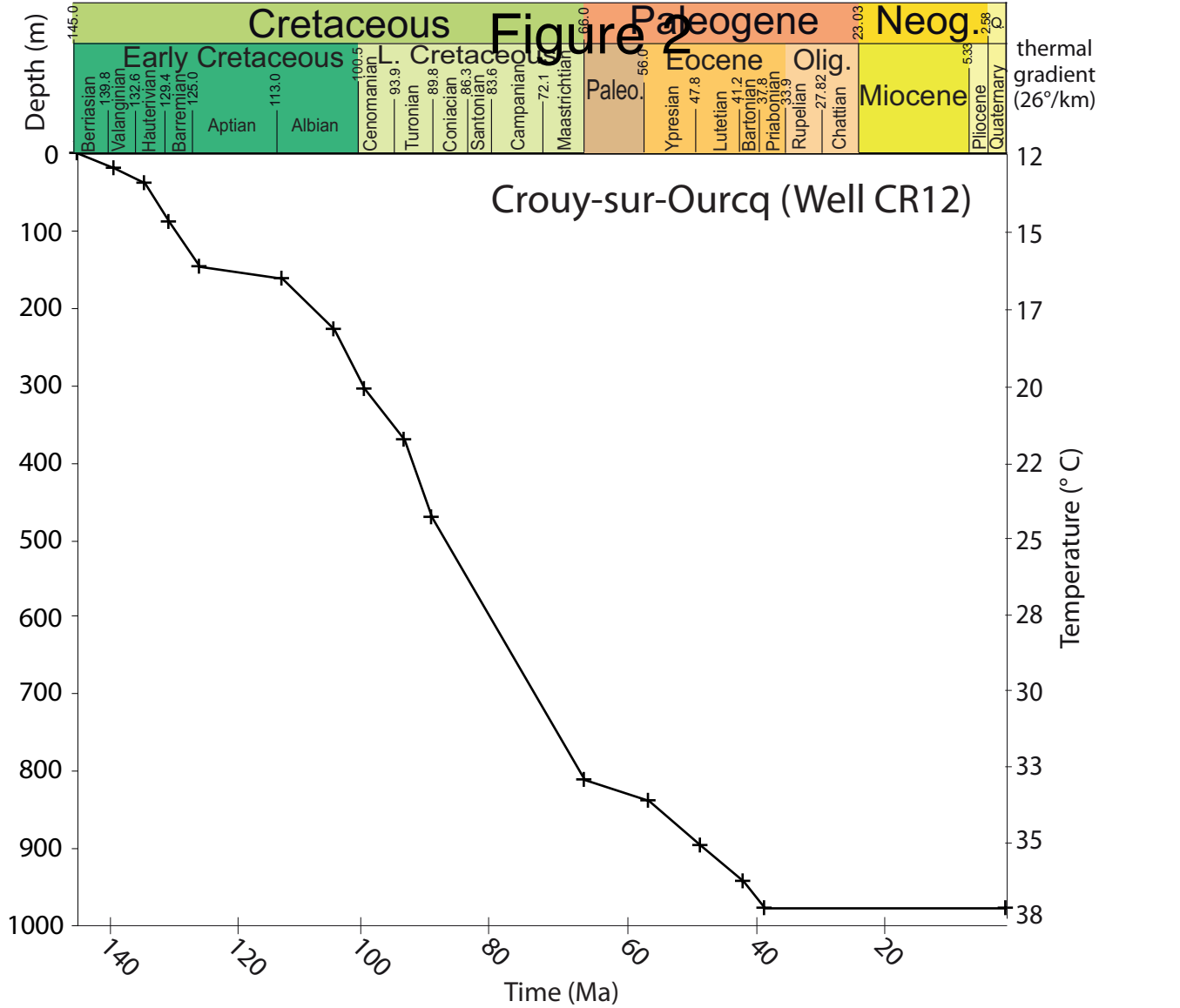
1254 **Table 2:** Average grain composition by automated point count analysis, estimated clay coat
1255 coverage, and clay fraction composition (XRD) by facies association.

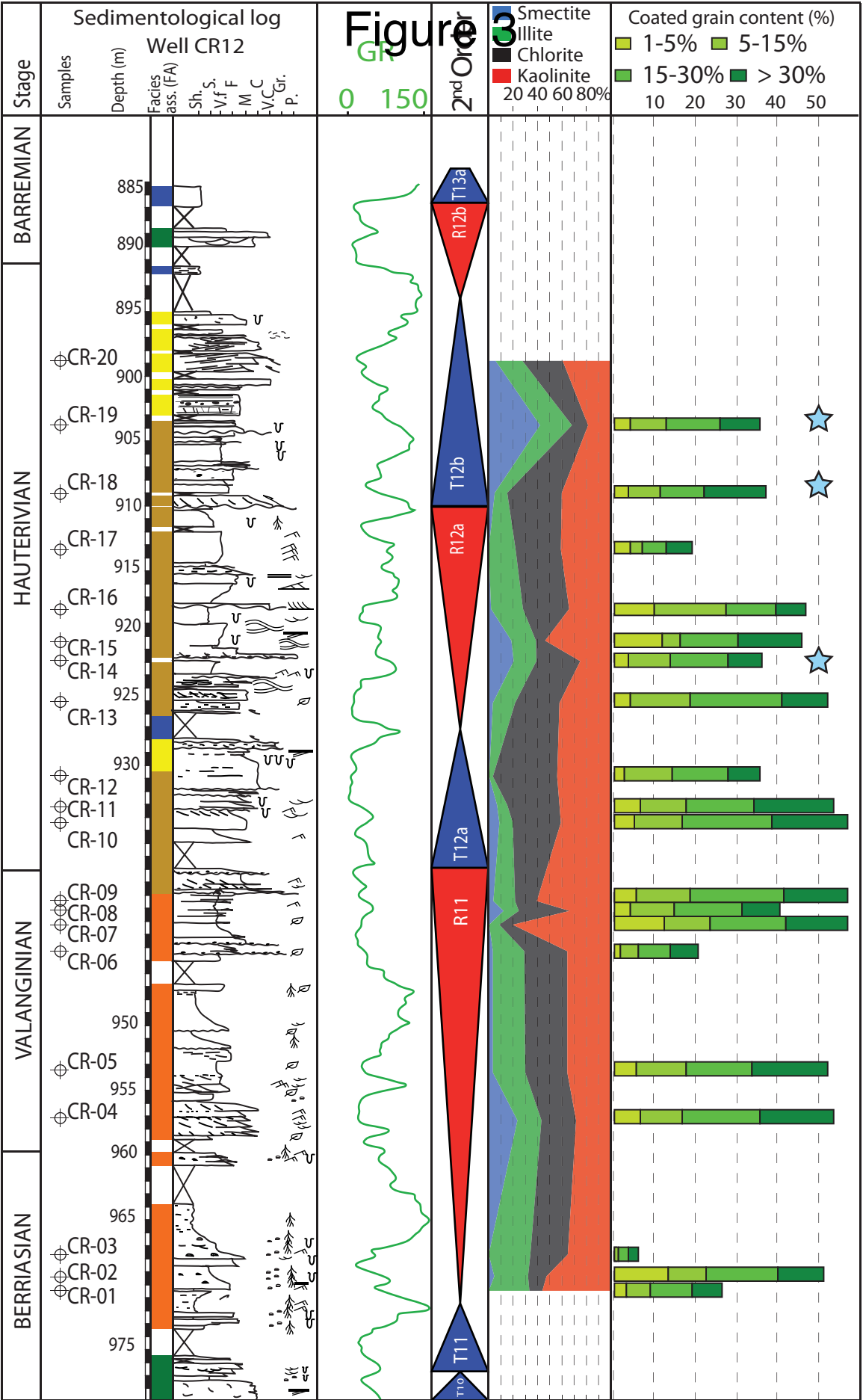
1256 **Table 3:** Chemical compositions of clay particles from clay coats within Wealden Group
1257 sandstones.

1258

1259 ¹GSA Data Repository item 20XXxxx, Supplemental Material Table S1 displaying sample
1260 description and petrographical/mineralogical composition (sample list, well location
1261 projection WGS84, sample depth, petrographical and clay mineral quantifications), is
1262 available online at www.geosociety.org/pubs/ft20XX.htm, or on request from
1263 editing@geosociety.org.





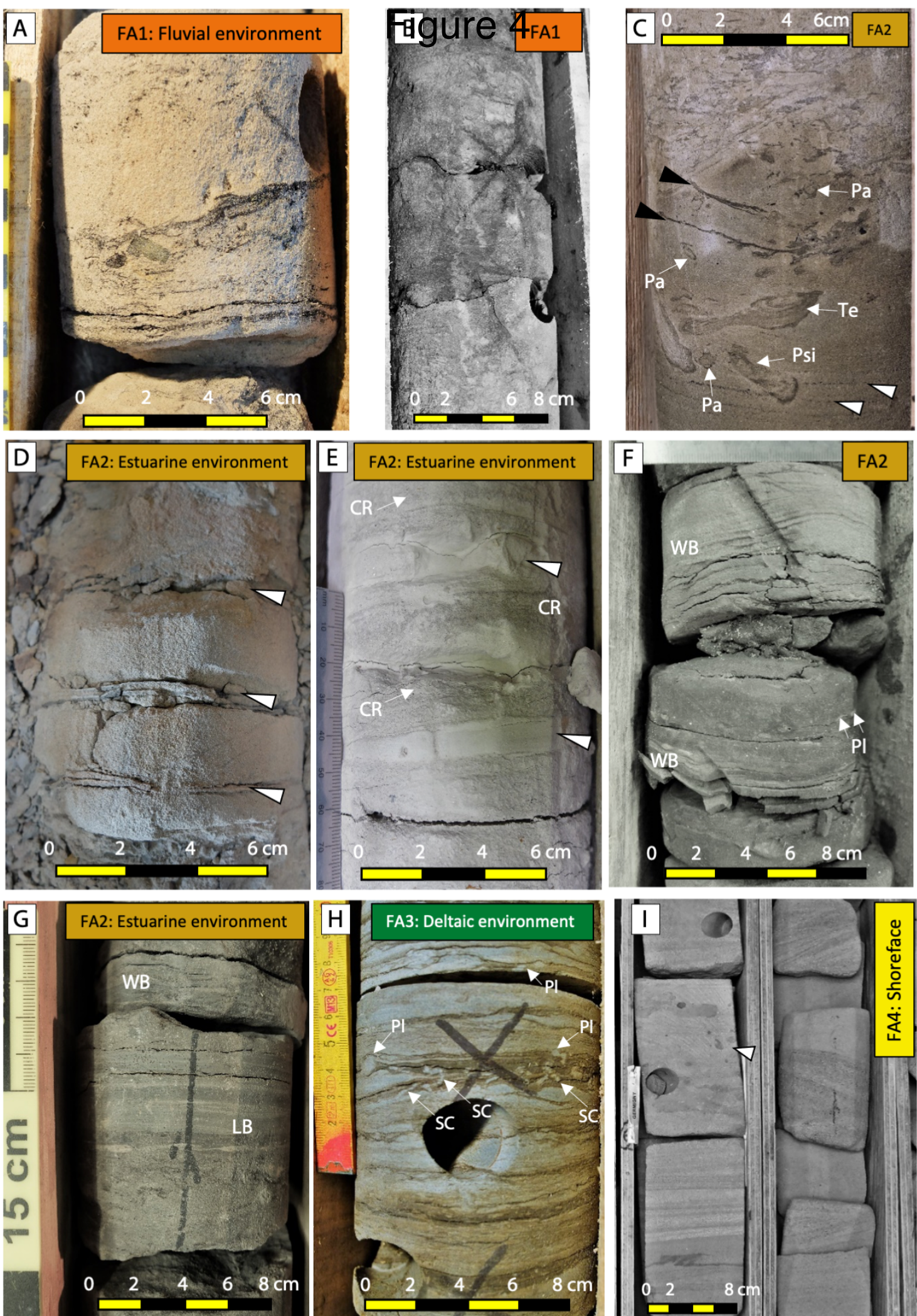


Facies associations

FA1: Fluvial FA2: Estuarine FA3: Delta FA4: Shoreface FA5: Offshore

Ripple Hummocky cross-stratification Roots Bivalves
Climbing ripple Lenticular bedding Leaves debris Berthierine
Trough-cross bedding Low angle stratification Bioturbation

Figure 4



Q

0 100

10 90

20 80

30 70

40 60

50 50

60 40

70 30

80 20

90 10

100 0

Subarkose

Sublitharenite

Quartzarenite

Arkose

Lithic arkose

litharenite

Feldspathic litharenite

Litharenite

FA1: Fluvial

FA2: Estuarine

FA3: Deltaic

FA5: Offshore

F 0 10 20 30 40 50 60 70 80 90 100 L

Figure 6

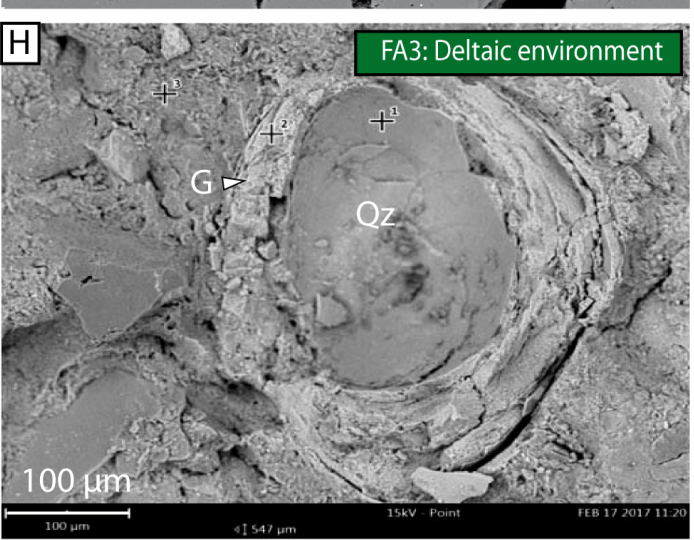
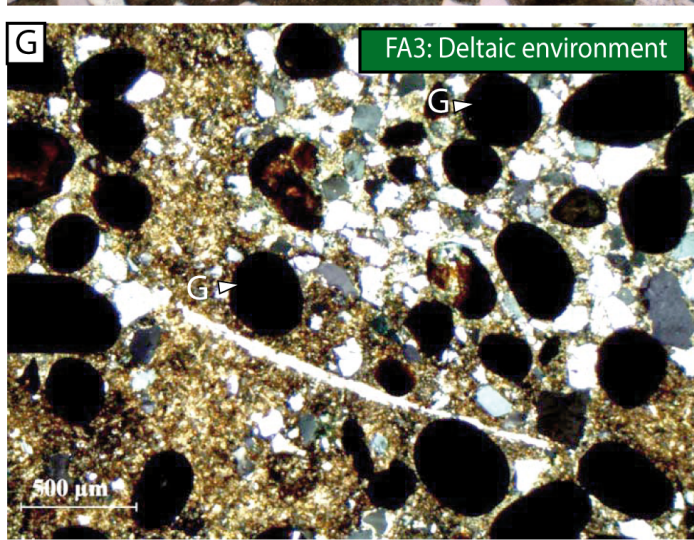
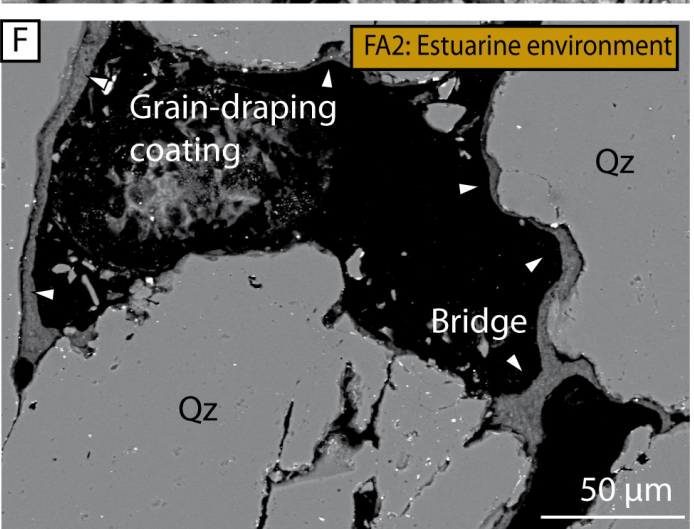
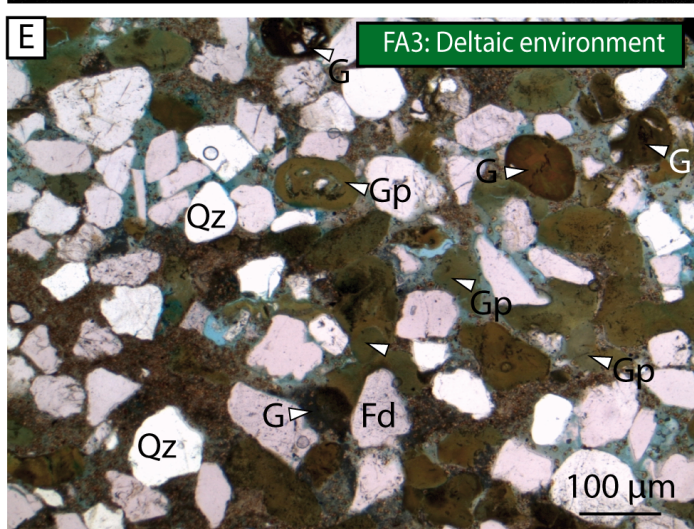
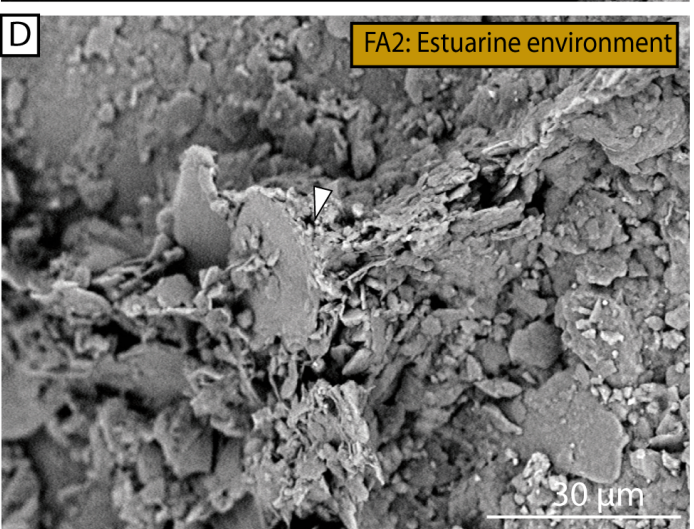
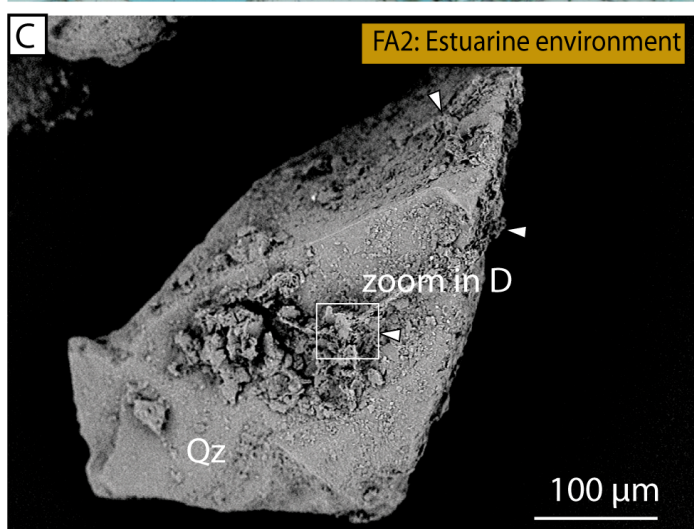
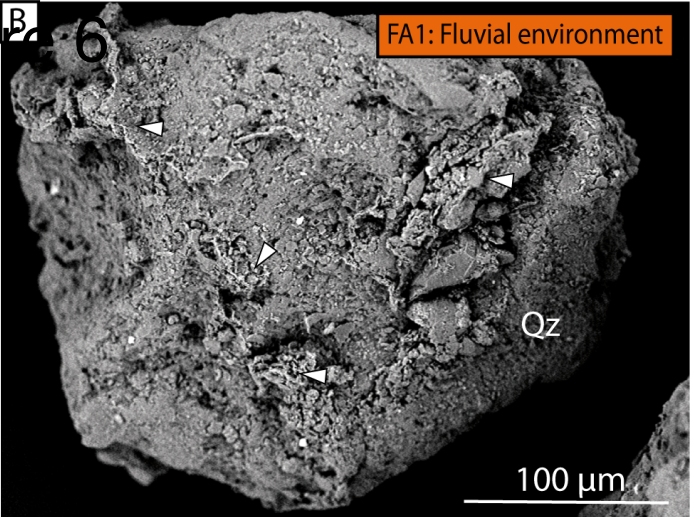
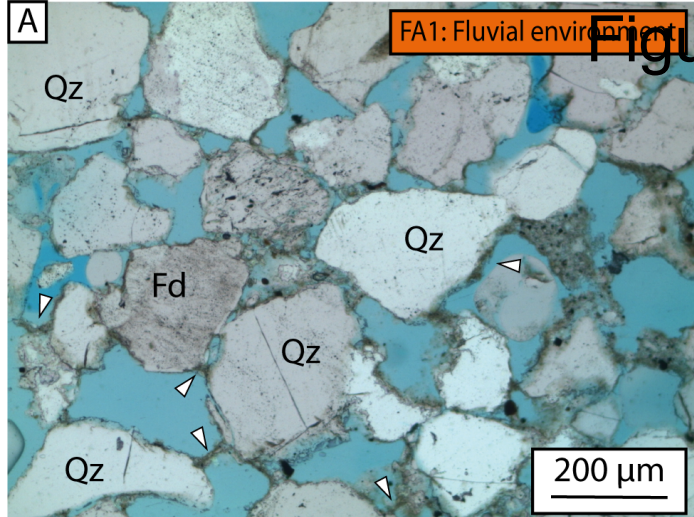


Figure 7

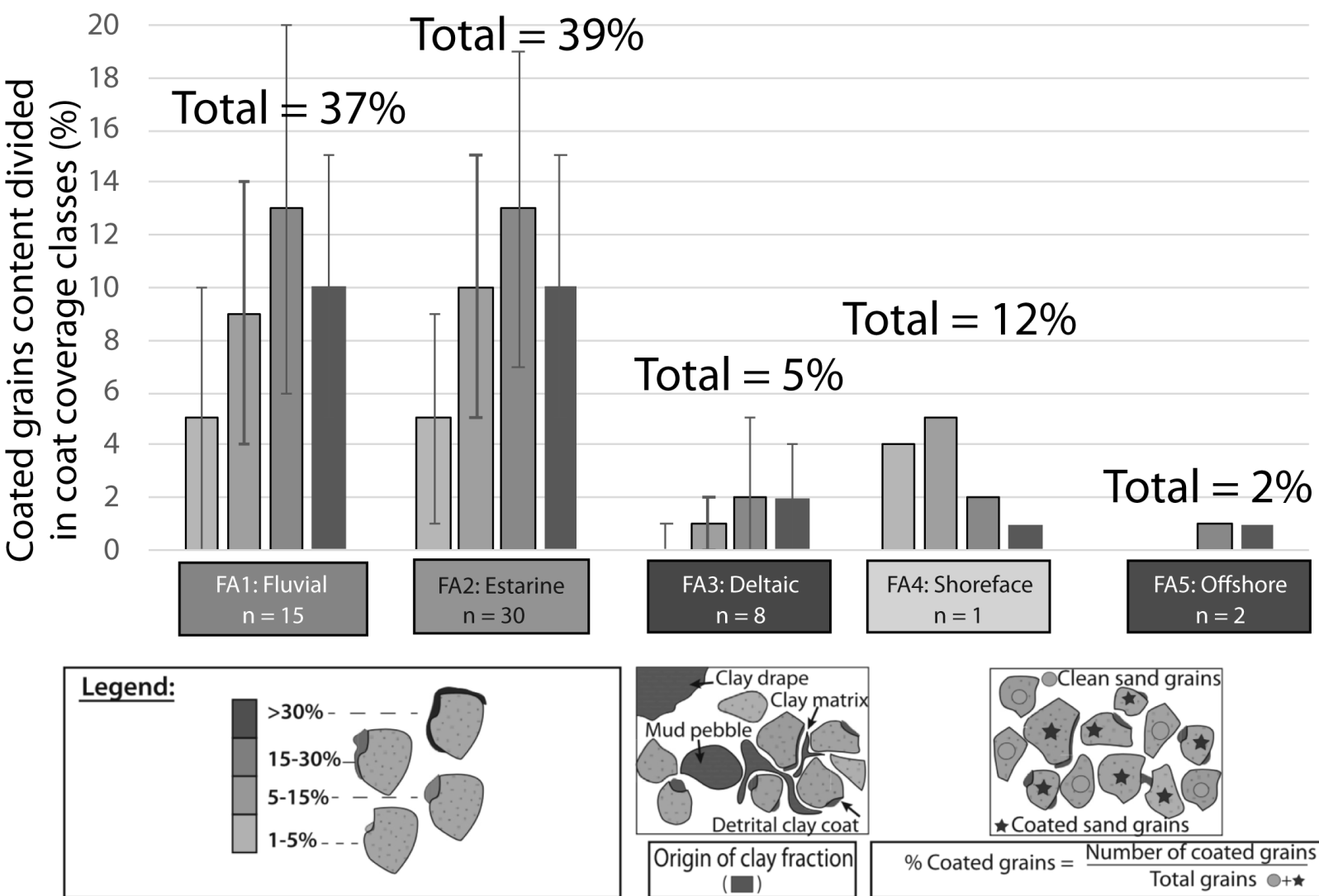


Figure 8

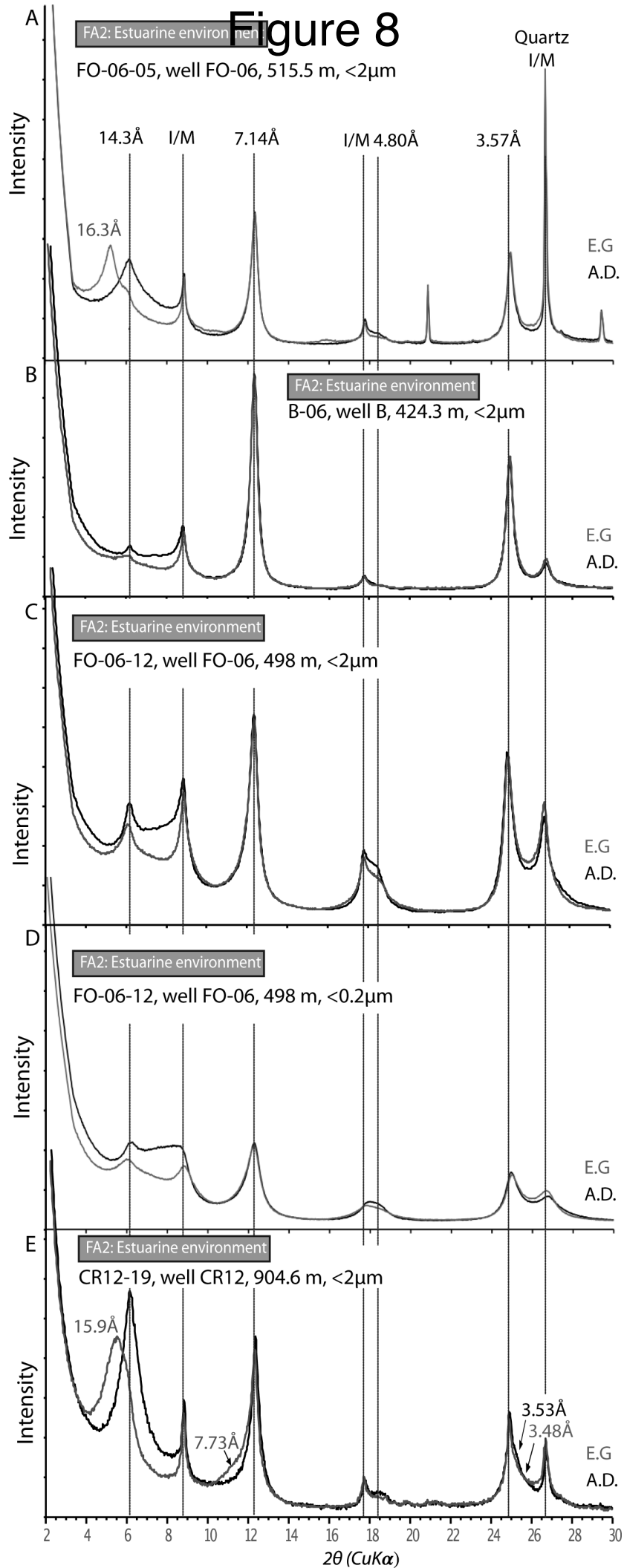


Figure 9

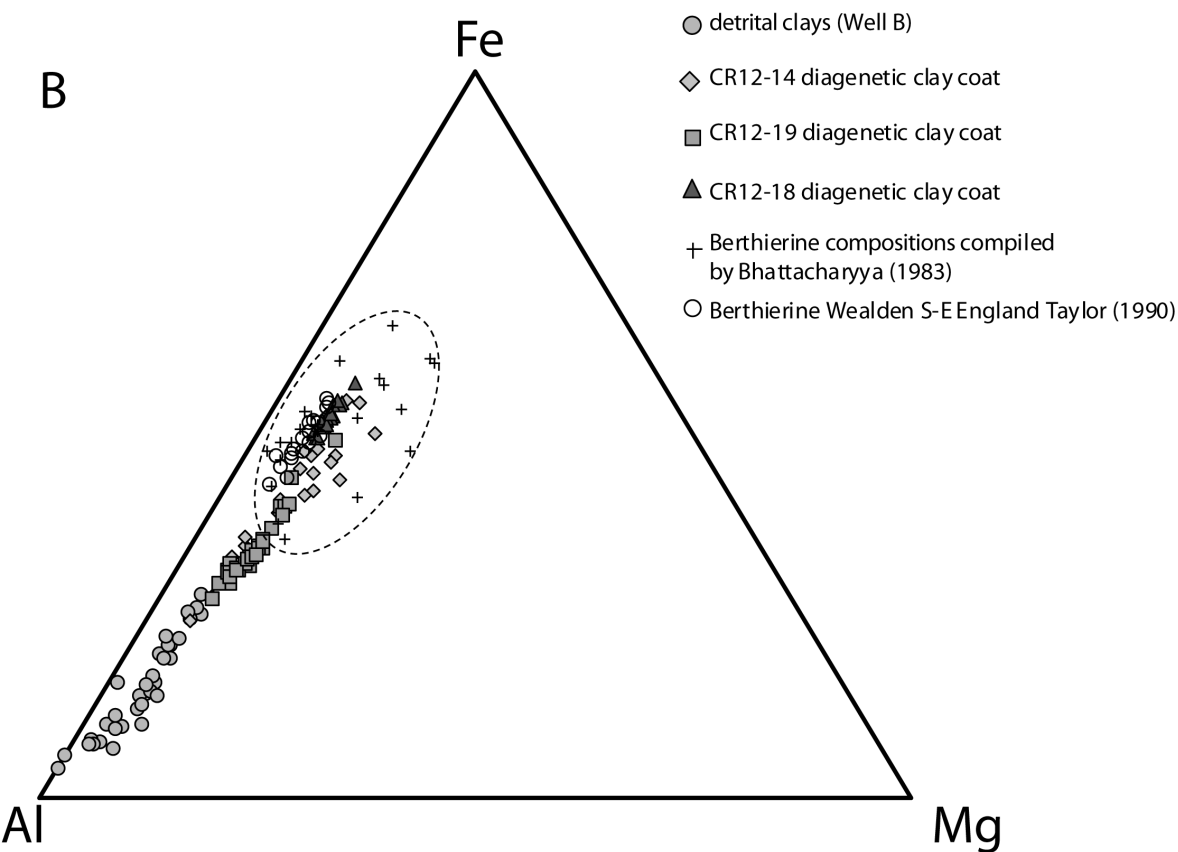
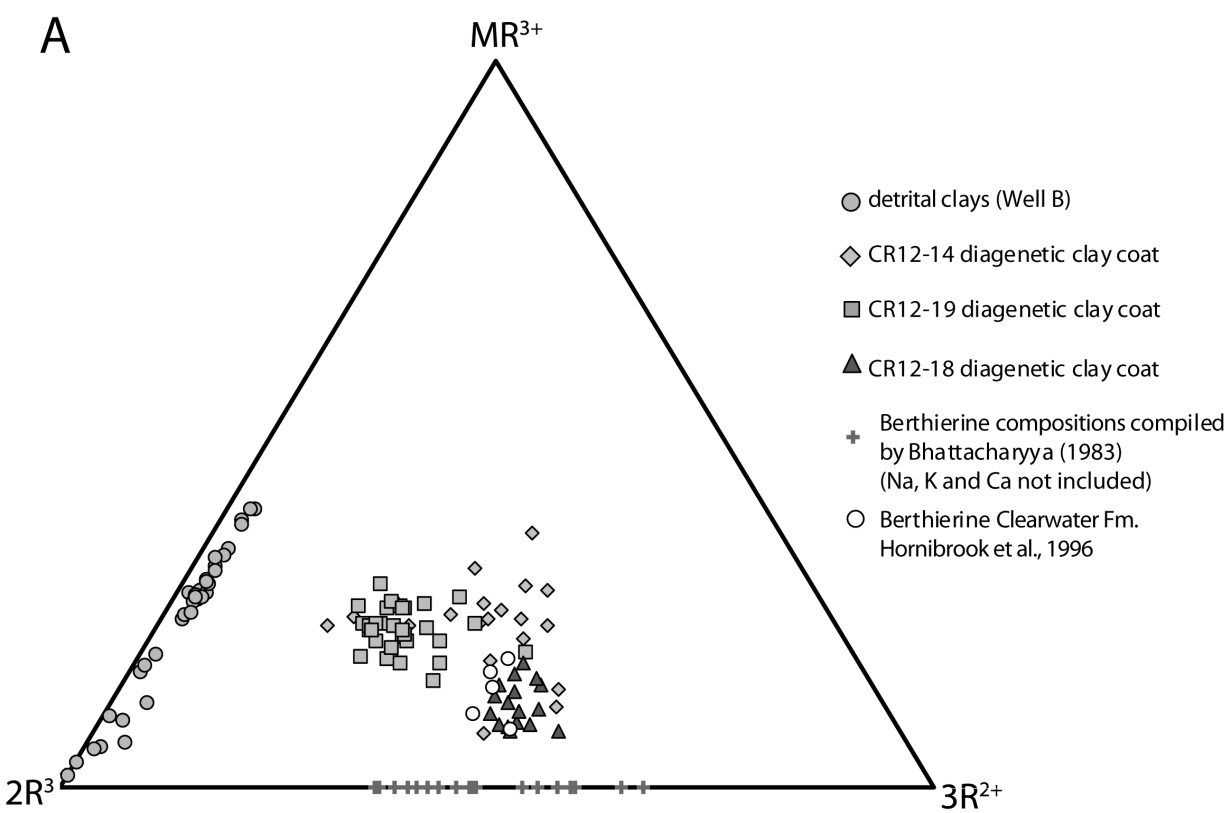


Figure 10

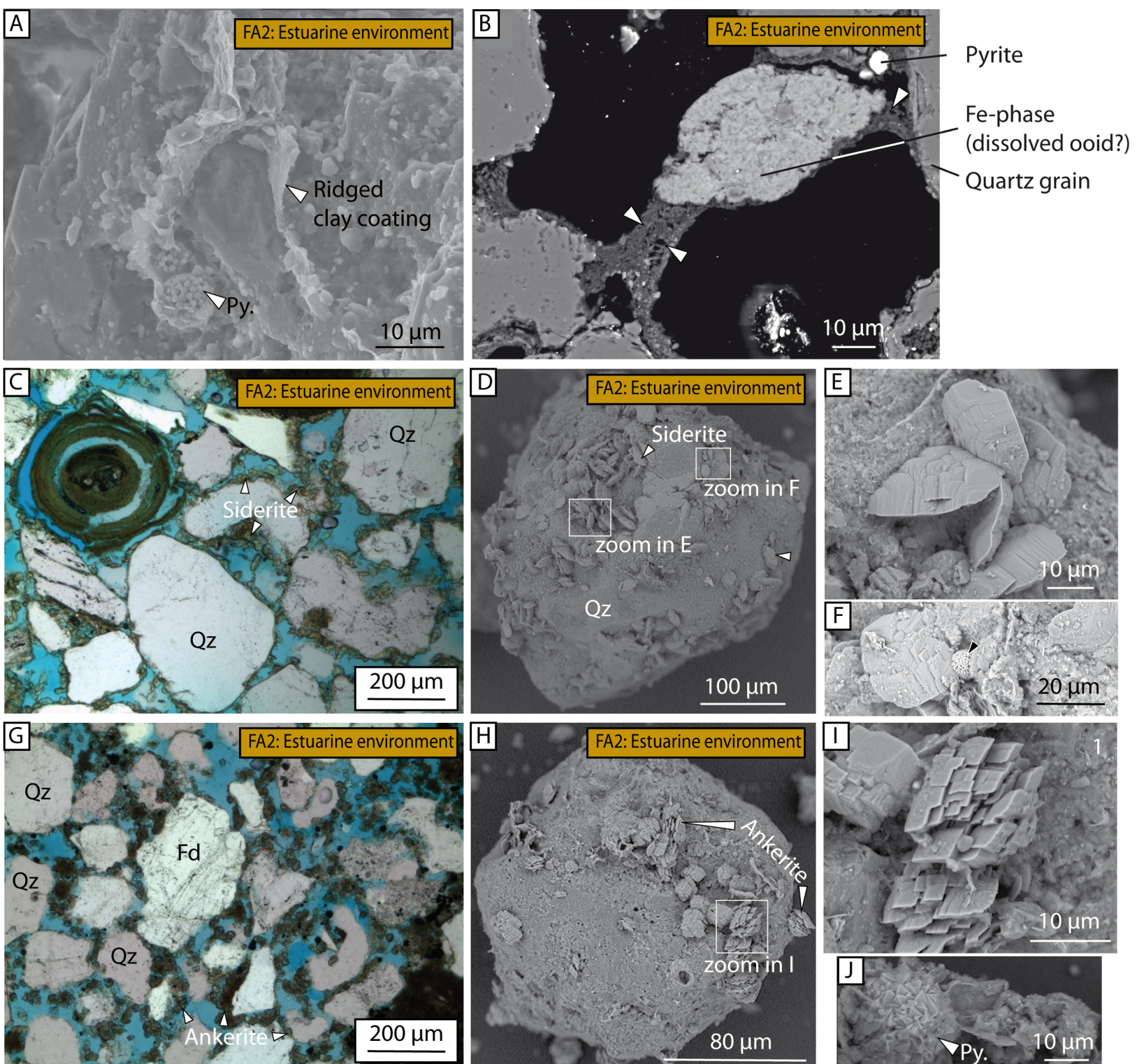


Figure 11

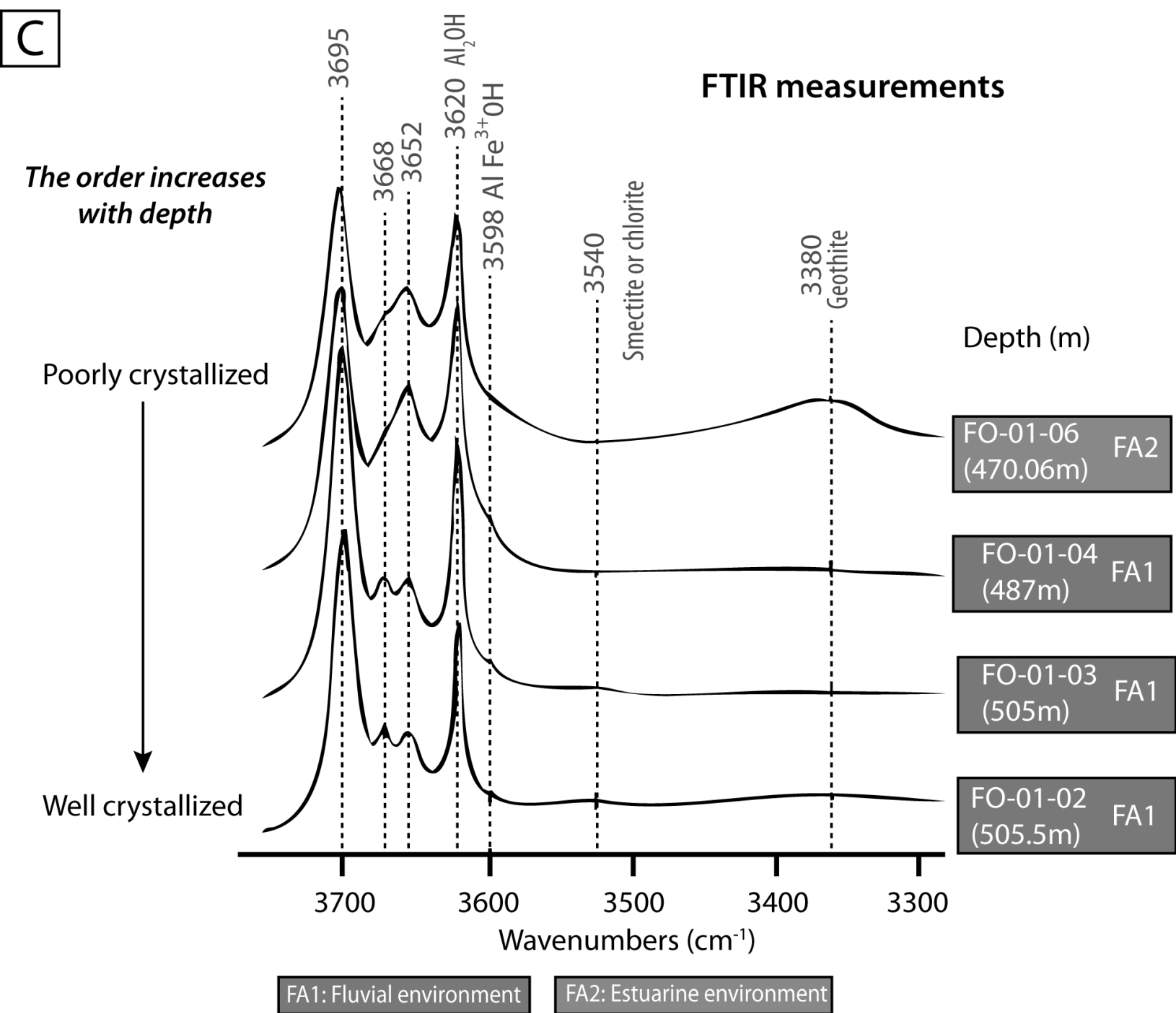
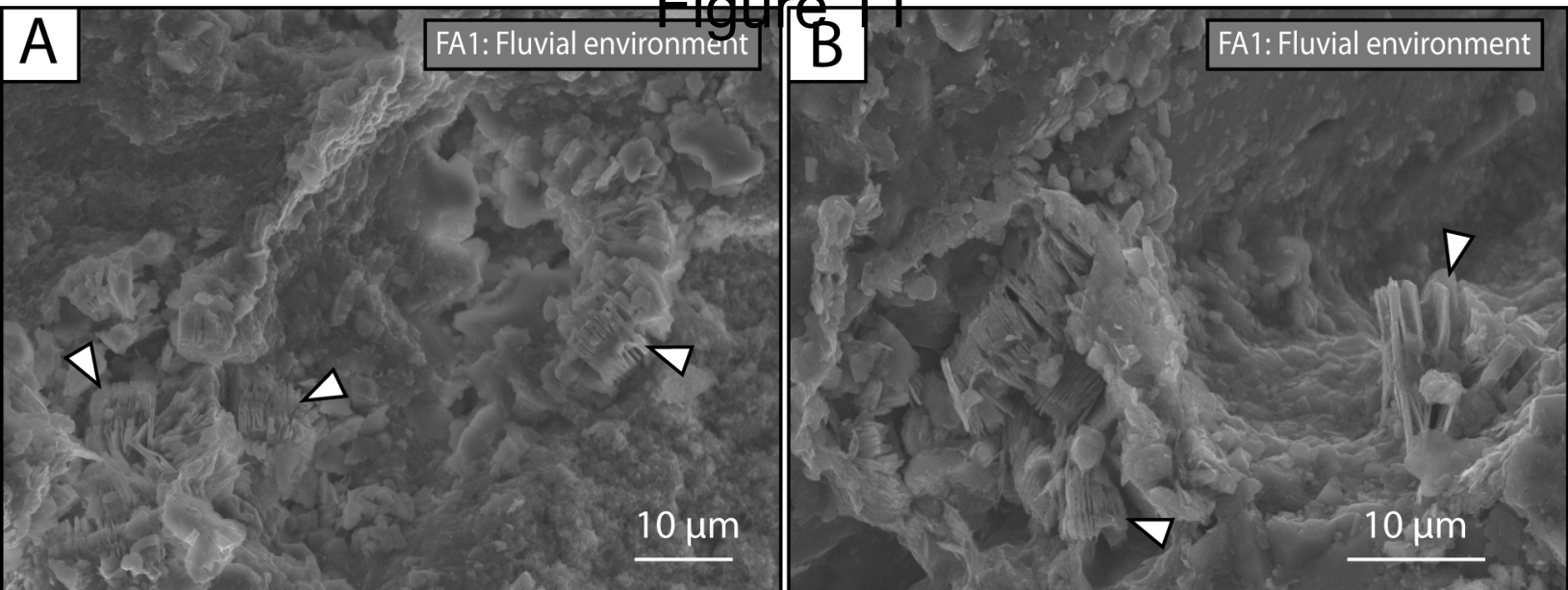


Figure 12

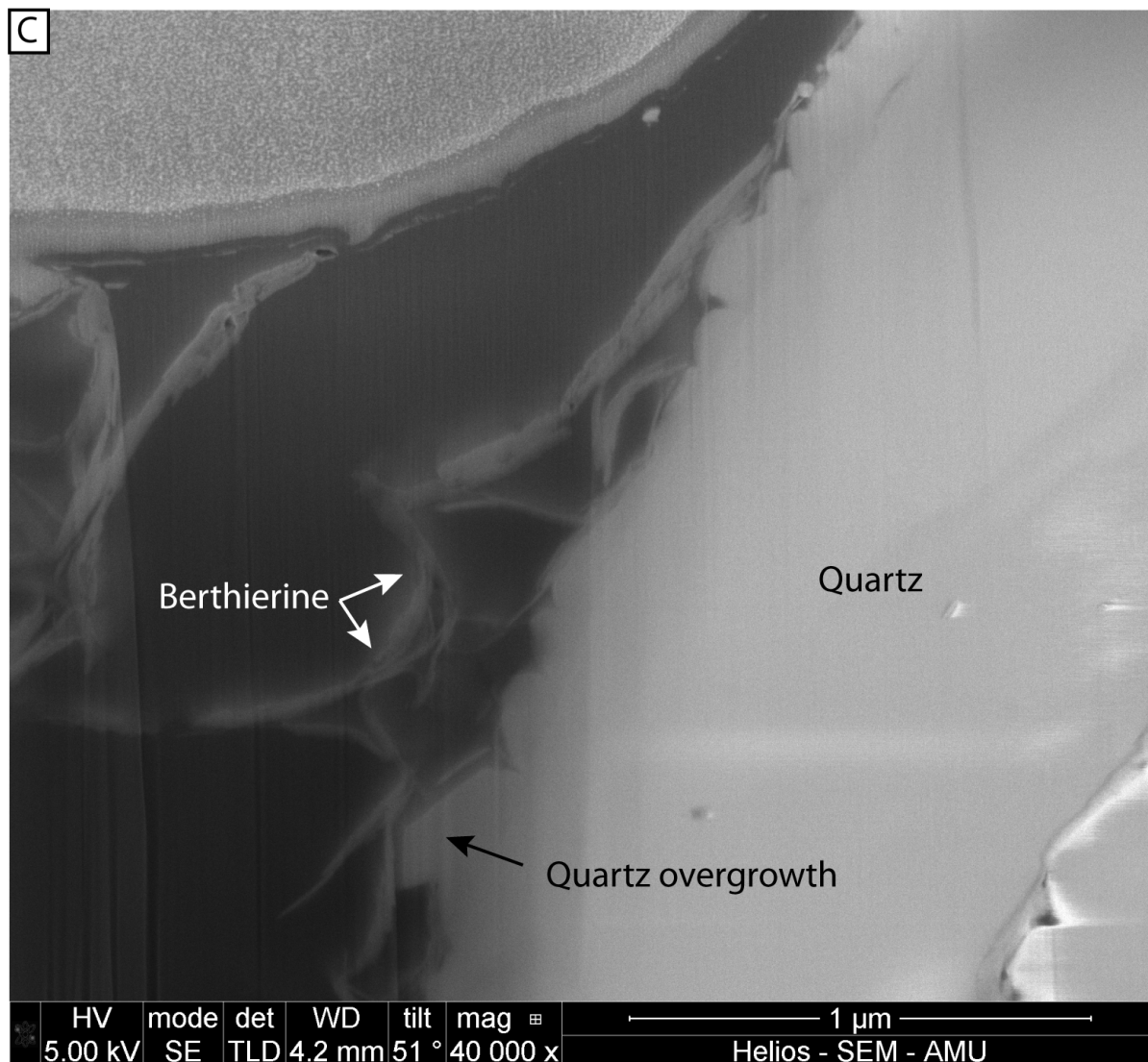
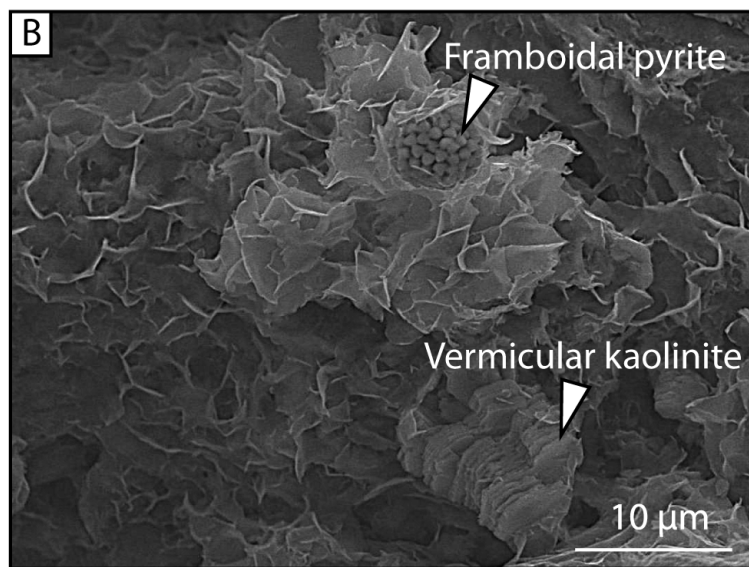
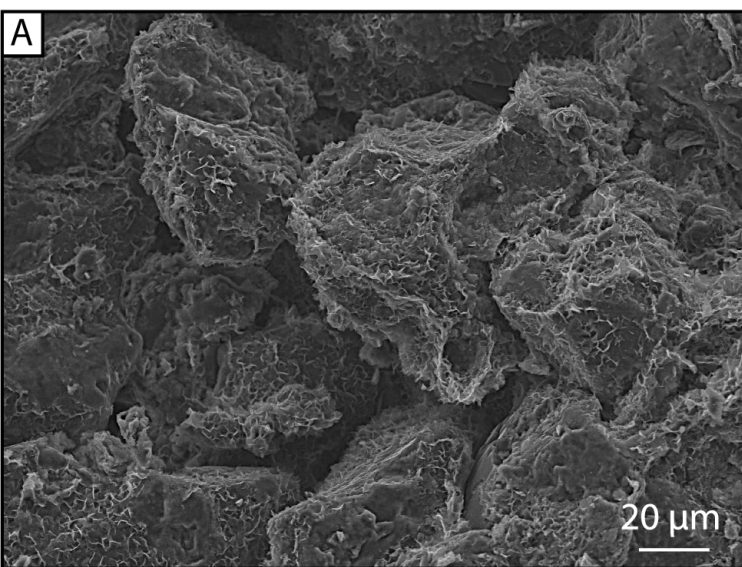


Figure 13

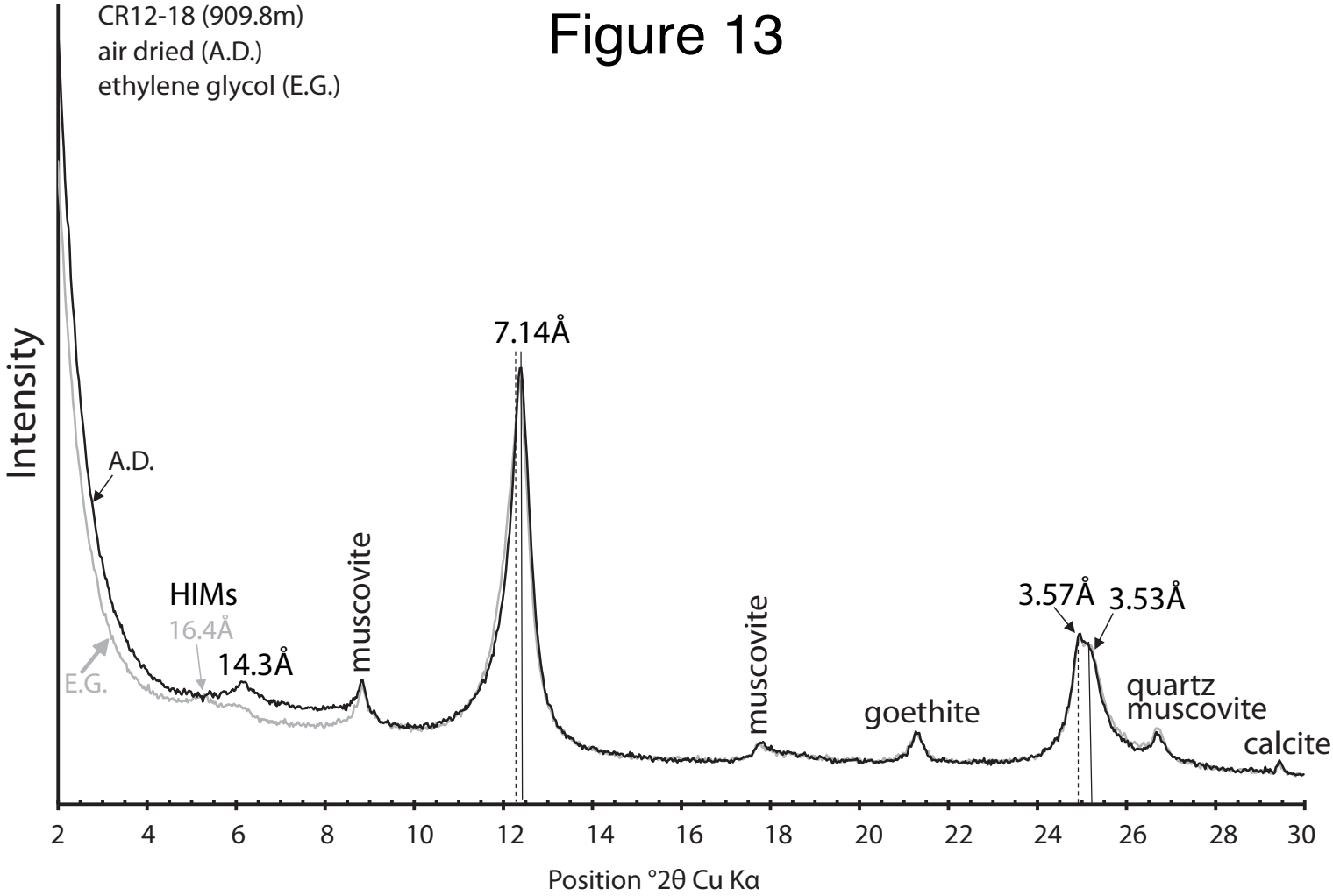
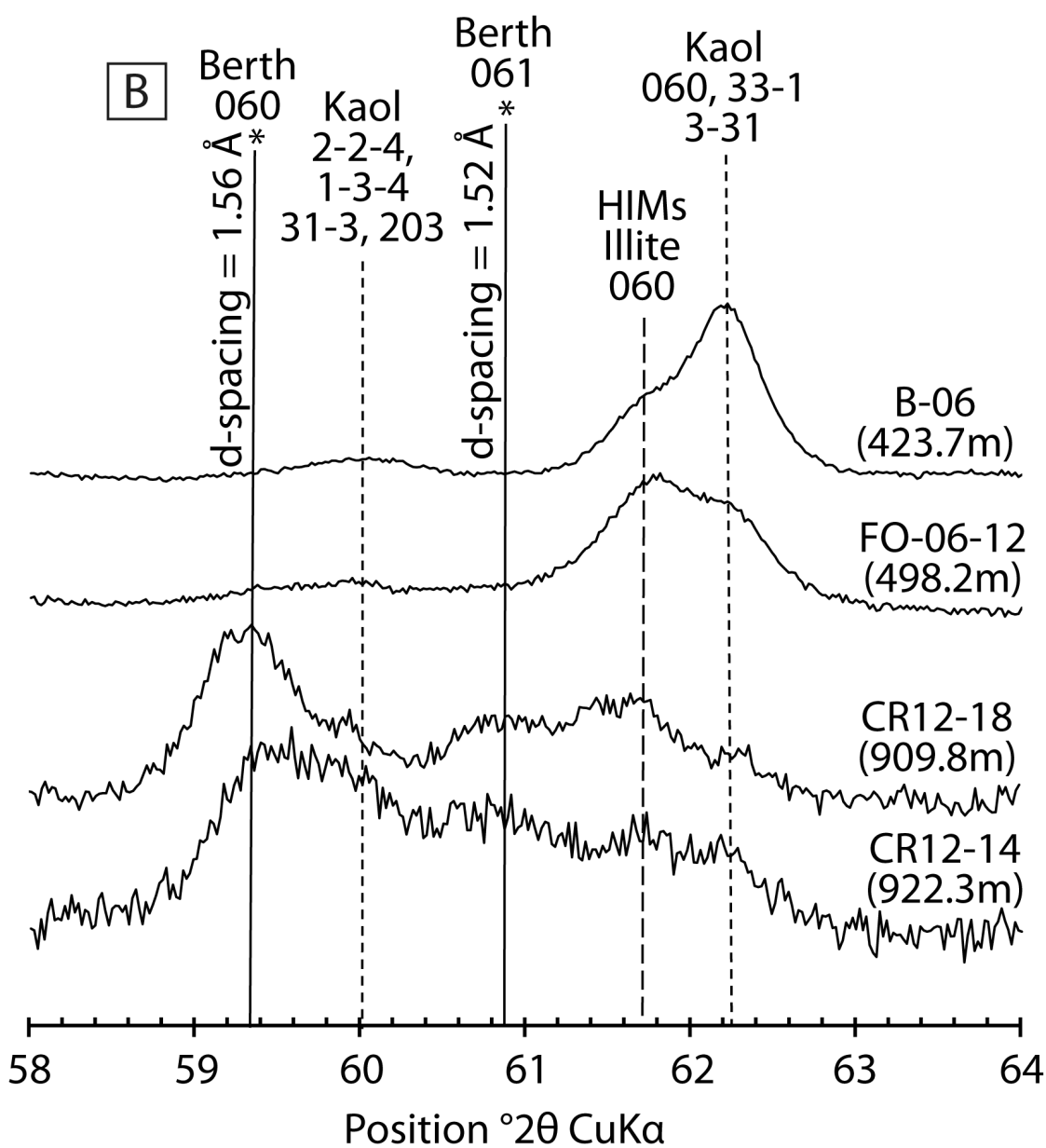
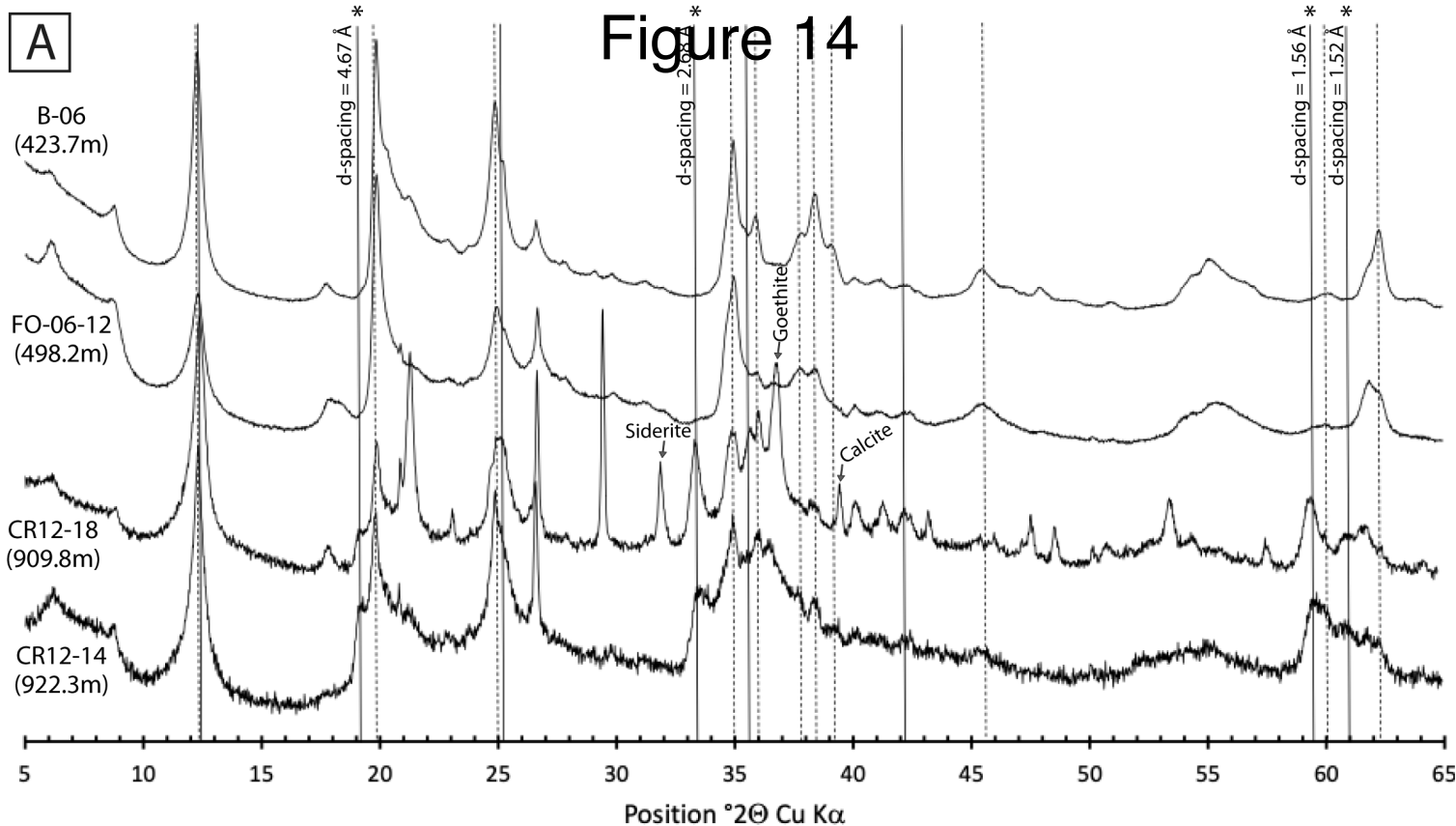


Figure 14



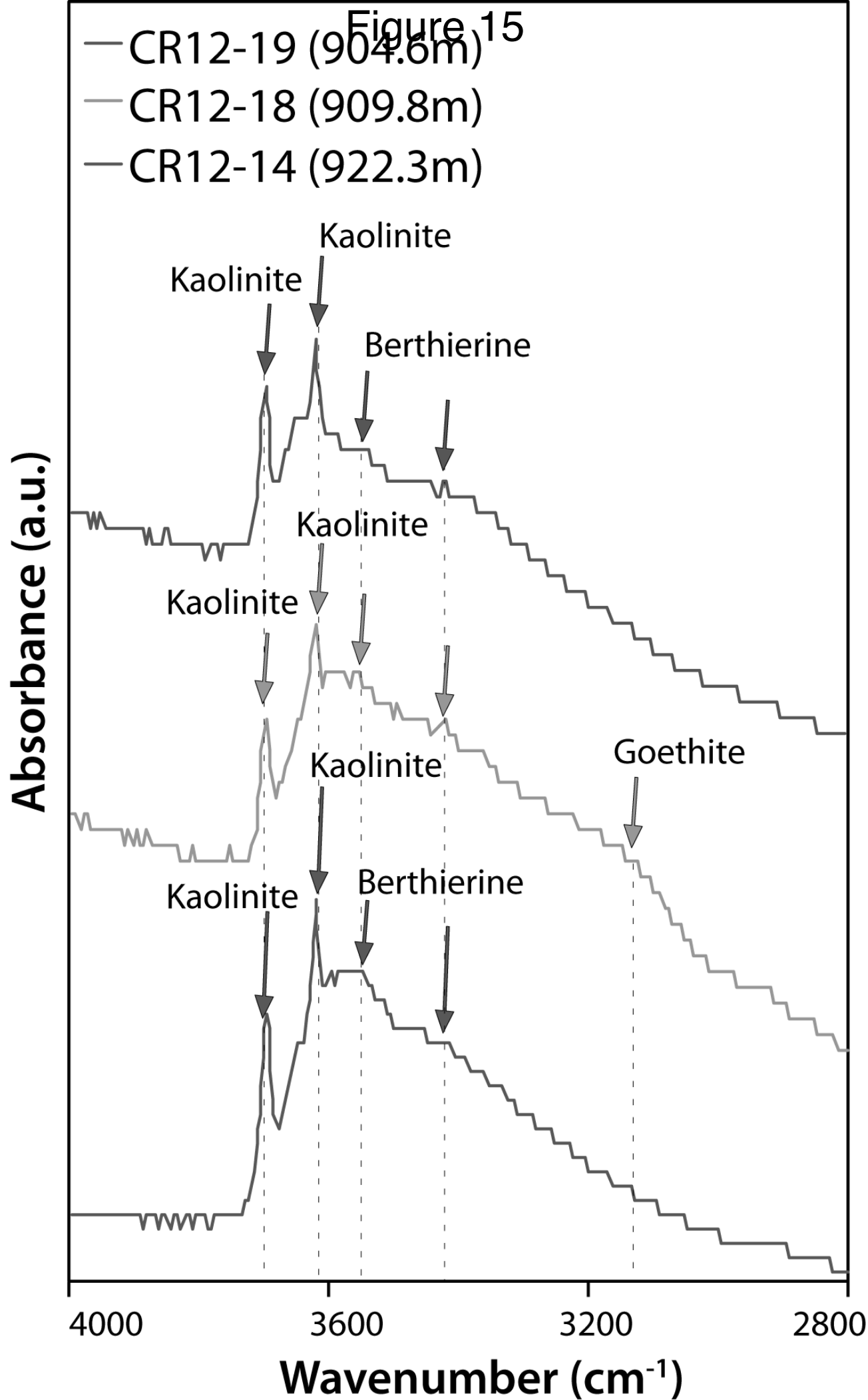
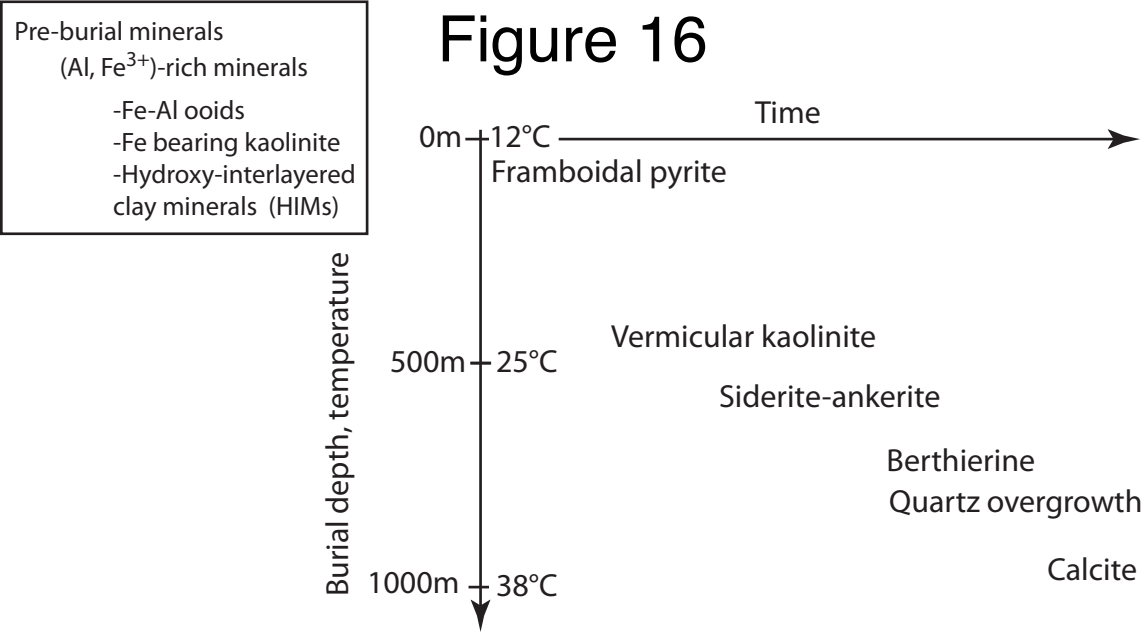


Figure 16



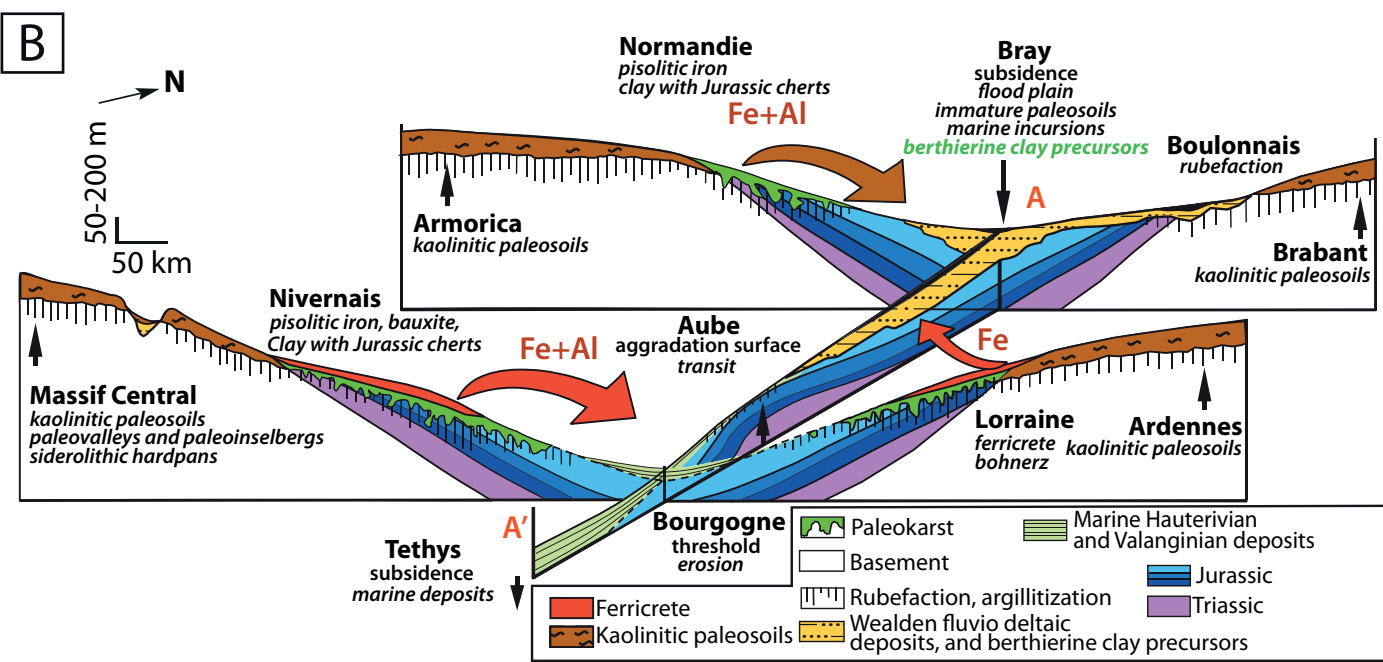
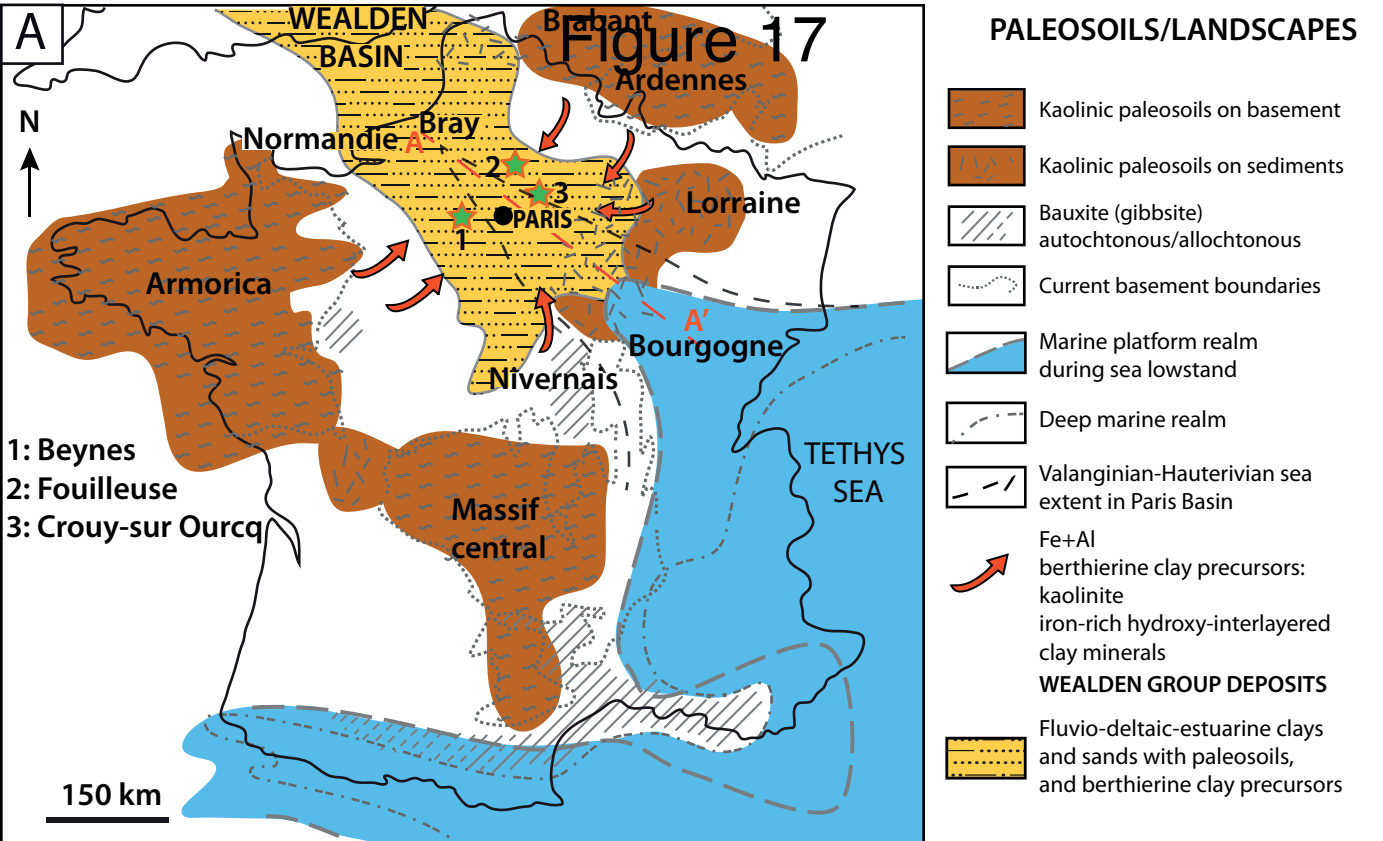


TABLE 1. SUMMARY OF F

| Facies | Facies |
|-----------------------------|--------|
| Association and environment | |
| FA1 FLUVIAL | |
| FA2 ESTUARINE | FA2a |
| | FA2b |
| | FA2c |
| FA3 DELTAIC | |
| FA4 SHOREFACE | |
| FA5 OFFSHORE | |

FACIES AND FACIES ASSOCIATION IDENTIFIED IN THE WEALDEN GROUP SAND

Description

1) Trough cross-bedded, medium to upper fine grained sandstones, locally conglomeratic. Numerous soft mud pebbles

2) Current-rippled upper fine to very fine grained sandstone with leaves and wood debris

3) Nodular siltstone & laminated siltstone, organic matter rich, and rooted silty mudstones and coal beds

Medium- to fine-grained sandstones, trough cross-bedding intercalated with thin clay layers. Foresets with clay drapes and organic matter debris. Reactivation surfaces. quartz, feldspars, mica ang. and surrounded grains. Rare glauconite ooids.

- 1) Flaser bedding composed of medium-grained, current-rippled sands with muddy flasers; (ii)
2) Fine grained, wavy bedding, with mm-to-cm fine-grained sandy rippled sands, draped by tidal slack water clay drapes,
3) Lenticular bedding with fine-grained sand ripples, mm of silty linsens and high-tide slack water clay drape.
-

Amalgamated clay drapes, organic matter rich with reed roots, with oxidized pedogenetic horizons. Stratification not always observed due to pedogenetic processes or due to reed roots.

1) Shales, silt and 10-50 mm current rippled very fine grained sandstones, with organic matter debris, synaeresis cracks, bioturbated.

2) Current-rippled fine grained sandstones (quartz and goethite ooids) to through cross bedded fine to medium sandstones. Foresets highlighted by organic matter debris.

3) Silty-claytones to silty sands, with no obvious sedimentary features, locally heavily bioturbated, with cm to pluri-cm intercalation of coal beds and locally rooted.

3) Silty-claytones to silty sands, with no obvious sedimentary features, locally heavily bioturbated, with cm to pluri-cm intercalation of coal beds and locally rooted.

Clean, well sorted, fine to medium / coarse grained sandstones. Low-angle, hummocky and swaley cross-bedding, locally well laminated or scrambled and heavily bioturbated. Occasional dispersed shell fragments. Marine shell lags.

Bioturbated shale with thin horizontal laminae of siltstone. Common bivalves and scattered shell fragments. Rich in organic carbon.

CLAYSTONES OF THE PARIS BASIN.

| Geometry | Bioturbations Fossils / microfossils |
|---------------------------------------------------------------------------------|----------------------------------------------------------------------------------------------------------------------------------------------------------------------------------------------------------------------------------------------------------------------------------------------------------------------------------------------------------------------------|
| Finning-upward, 20-50 cm bedsets | Roots / Fresh water algae (<i>Botryococcus spp.</i>) continental spores <i>Densioisporites spp</i> wood & leaf debris |
| Infra-cm to pluri-cm beds, up to 70 cm bedsets | |
| Frequently deformed, roots, up to 2-3 meters | Roots, wood and leaf debris, coal intervals |
| 10-25 small tidal dunes, reactivation surfaces. | See below |
| mm to several mm thick beds. Amalgamated in bedsets up to 15 to 50 cm thick. | Rare bioturbations, mainly <i>planolites</i> Firm grounds / <i>Glossifungites</i> (917-914m) - Iron-oxydes Continental input: pollens and spores <i>Classopolis spp.</i> or <i>Exesipollenites spp.</i> Marine input: <i>Muderongia crucis</i> or <i>Stiphrosphaeridium anthophorum</i> or dinoflagellate <i>Rhynchodiniopsis fimbriat</i> (Rusciadelli, 1996) |
| mm-thick laminae. Stratification | Reed roots |
| Planar bedding | Rare bioturbation, <i>planolites</i> Marine microfossils such as dinoflagellate <i>Muderongia crucis</i> or <i>Oligosphaeridium asterigerum</i> |
| 15-50 cm bedsets, dipping angle 5-10° Coarsening-up trend, 20-80 cm bedsets | |
| 20-250 cm bedsets coal intercalation | <i>Planolites</i> , <i>skolithos linearis</i> , <i>teichichnus</i> roots |
| Finning-up bed sets, with erosive base | None. Roots ? |
| Frequent reactivation surfaces, 35 cm to 200 cm bedsets | <i>Skolithos</i> , frequent <i>ophiomorpha</i> ichnofacies |
| Massive claystones intervals (1 to 2m thick) - Low core recovery | Bivalves, oncoids Coccoliths, foraminifera |

Interpretation

Fluvial channels, with
levees - flood plain

Tidal bars

Tidal flats

Supra-tidal marsh

Prodelta

Prograding Lower delta

Delta plain

Distributary channel

Wave action
Storm deposits
Lower to Upper
Shoreface

Offshore, open marine

TABLE 2. COMPOSITION OF QUARTZ, FELDSPAR, LITHIC AND CLAY COATS IN SAMPLES ACCORDING TO FACIES.

| Facies Associations | Grain composition | | | | | Coated grain content and coat coverage classes (percentage of the outer surface coated) | | | | | Clay fraction content and clay assemblage within clay fraction | | | |
|------------------------|-------------------|------------------|-------------------------|--------------|--------|-----------------------------------------------------------------------------------------------|-----------|------------|--------------|-------------------------------|-------------------------------------------------------------------|----------|---------------|--------------------|
| | Quartz (%) | Feldspars (%) | Lithic grains (%) | Clays (%) | Others | 1– 5% | 5– 15% | 15– 30% | > 30 % | Total coated grains (%) | % Smectite | % Illite | % Chlorite | % Kaolin ite |
| FA1 | 41 | 7 | 12 | 12 | 29 | 5 | 9 | 13 | 10 | 37 | 7 | 23 | 25 | 45 |
| FA2 | 39 | 8 | 12 | 9 | 32 | 5 | 10 | 13 | 10 | 39 | 10 | 19 | 26 | 45 |
| FA3 | 33 | 5 | 9 | 9 | 43 | 0 | 1 | 2 | 2 | 5 | 9 | 33 | 26 | 32 |
| FA4 | 30 | 5 | 8 | 18 | 39 | 4 | 5 | 2 | 1 | 12 | 3 | 20 | 29 | 48 |
| FA5 | 27 | 2 | 3 | 23 | 46 | 0 | 0 | 1 | 1 | 2 | 0 | 33 | 22 | 44 |
| Total/Mean | 34 | 5 | 9 | 14 | 38 | 3 | 5 | 6 | 5 | 19 | 6 | 26 | 26 | 43 |

TABLE 3. CHEMICAL COMPOSITIONS OF CLAY PARTICLES FROM CLAY COATS WITHIN WEALDEN GROUP SANDSTONES.

| | 1 | 2 | 3 | 4 | 5 | 6 | 7 | 8 |
|--------------------------------|-------|-------|-------|-------|-------|-------|-------|-------|
| SiO ₂ | 45.59 | 52.90 | 42.51 | 46.53 | 26.37 | 28.60 | 27.36 | 30.10 |
| Al ₂ O ₃ | 36.47 | 24.44 | 26.47 | 21.84 | 16.79 | 19.12 | 18.12 | 16.25 |
| FeO | 0.00 | 0.00 | 0.00 | 0.00 | 38.38 | 34.34 | 36.47 | 34.45 |
| Fe ₂ O ₃ | 3.41 | 4.36 | 10.64 | 12.30 | 0.00 | 0.00 | 0.00 | 0.00 |
| MgO | 0.14 | 0.67 | 1.16 | 1.15 | 2.94 | 2.62 | 2.63 | 3.39 |
| TiO ₂ | 0.10 | 0.53 | 0.72 | 0.59 | 0.00 | 0.00 | 0.04 | 0.04 |
| MnO | 0.05 | 0.07 | 0.06 | 0.00 | 0.38 | 0.12 | 0.12 | 0.26 |
| Na ₂ O | 0.05 | 0.31 | 0.34 | 0.18 | 0.14 | 0.14 | 0.05 | 0.62 |
| K ₂ O | 0.16 | 1.55 | 3.72 | 3.17 | 0.66 | 0.69 | 0.82 | 0.76 |
| CaO | 0.03 | 1.17 | 0.38 | 0.24 | 0.34 | 0.37 | 0.39 | 0.13 |

Note: Analyses 1 to 4 are representative of pre-burial clay coats (1: detrital kaolinite, sample B-6, well B; 2: smectite-rich detrital clay material, sample B-5, well B; 3–4: hydroxy-interlayered-rich detrital clay material, sample B-12, well B). Analyses 5 to 8 are representative of diagenetic clay coats (authigenic berthierine); analyses 5 to 7: sample CR12-18, well CR1, analyses 8: sample CR12-14, well CR12. Compositions were calculated from Energy Dispersive X-ray analyses (EDS) in the SEM and expressed in oxide weight percent. For easier comparison, they were normalized to a sum of 86% (which is the theoretical sum of oxide weight percent for dehydrated kaolinite and berthierine) for easier comparison. Total iron has been arbitrarily considered as ferric in detrital clays and as ferrous in authigenic berthierine.